# CD4 T cell Responses in the CNS during SIV infection

Sonny R Elizaldi[1], Anil Verma[2], Zhong-Min Ma[3], Sean Ott[3], Dhivyaa Rajasundaram[4], Mackenzie L. Cottrell[5], Angela D. M. Kashuba[5], Zandrea Ambrose[6], Jeffrey D. Lifson[7], John H. Morrison[3,8], Smita S. Iyer[2,3,9]

[1]Graduate Group in Immunology, UC Davis, CA, USA; [2]Department of Pathology, School of Medicine, University of Pittsburgh, PA, USA; [3]California National Primate Research Center, UC Davis, CA, USA; [4]Department of Pediatrics, School of Medicine, University of Pittsburgh, PA,USA; [5]Eshelman School of Pharmacy, University of North Carolina, Chapel Hill, NC, USA; [6]Department of Microbiology and Molecular Genetics, School of Medicine, University of Pittsburgh, PA, USA; [7]AIDS and Cancer Virus Program, Frederick National Laboratory, Frederick, MD, USA; [8]Department of Neurology, School of Medicine, UC Davis, CA,USA; [9]Department of Pathology, Microbiology, and Immunology, School of Veterinary Medicine, UC Davis, CA,USA

Corresponding author/Lead contact: siyer.3@pitt.edu

## ABSTRACT

Virologic suppression with antiretroviral therapy (ART) has significantly improved health outcomes for people living with HIV, yet challenges related to chronic inflammation in the central nervous system (CNS) - known as Neuro-HIV- persist. As primary targets for HIV-1 with the ability to survey and populate the CNS and interact with myeloid cells to co-ordinate neuroinflammation, CD4 T cells are pivotal in Neuro-HIV. Despite their importance, our understanding of CD4 T cell distribution in virus-targeted CNS tissues, their response to infection, and potential recovery following initiation of ART remain limited. To address these gaps, we studied ten SIVmac251-infected rhesus macaques using an ART regimen simulating suboptimal adherence. We evaluated four macaques during the acute phase pre-ART and six during the chronic phase. Our data revealed that HIV target CCR5+ CD4 T cells inhabit both the brain parenchyma and adjacent CNS tissues, encompassing choroid plexus stroma, dura mater, and the skull bone marrow. Aligning with the known susceptibility of CCR5+ CD4 T cells to viral infection and their presence within the CNS, high levels of viral RNA were detected in the brain parenchyma and its border tissues during acute SIV infection. Single-cell RNA sequencing of CD45+ cells from the brain revealed colocalization of viral transcripts within CD4 clusters and significant activation of antiviral molecules and specific effector programs within T cells, indicating CNS CD4 T cell engagement during infection. Despite viral suppression with ART, acute infection led to significant depletion of CNS CD4 T cells, persisting into the chronic phase. These findings underscore the functional involvement of CD4 T cells within the CNS during SIV infection, enhancing our understanding of their role in establishing CNS viral presence. Our results offer insights for potential T cell-focused interventions while also underscoring the challenges in eradicating HIV from the CNS, even with effective ART.

## AUTHOR SUMMARY

Antiretroviral therapy (ART) has improved health outcomes of people living with HIV. However, there are still challenges, especially in the central nervous system (CNS), where ongoing inflammation can lead to neurological disorders. Our study focused on understanding the role of CD4 T cells in the brain during HIV infection and treatment. We used a model with SIV-infected rhesus monkeys to study the AIDS virus in the brain and surrounding tissues. We discovered that a subset of CD4 T cells, which are vulnerable to HIV, are present throughout the CNS. During the early stages of infection, we noticed high levels of the virus in both the brain and nearby tissues. By examining these CD4 T cells at a single-cell level, we found that they actively respond to the virus by activating specific antiviral effector functions to fight it. Although ART controlled virus replication in the brain, CD4 T cells were continuously depleted, indicative of immune perturbations. Overall, our study helps us understand the role of CD4 T cells within the CNS during both acute and chronic HIV infection. This knowledge could help us develop new ways to target the virus in the CNS and devise treatments for complications related to Neuro-HIV.

## INTRODUCTION

Improved access to early and sustained antiretroviral therapy (ART) has significantly enhanced the life expectancy of people living with HIV (PLWH). Studies show that immediate ART initiation upon diagnosis is the most effective approach to achieving positive long-term health outcomes [1-4]. However, often, ART is not initiated until well after clinical symptoms have become evident [5, 6]. Delay in treatment initiation leads to systemic viral dissemination and a decline in CD4 T cell counts, which puts PLWH at a higher risk of developing chronic inflammatory disorders that can affect multiple organ systems, particularly the brain [7, 8]. Indeed, the severity of cognitive impairment at the time of ART initiation is the strongest predictor of persistent neurocognitive deficits despite long-term ART, underscoring the significance of early-stage viral spread and neuroinflammation in the disease process and indicating that substantial neurological damage is inflicted early following infection [9-12]. As the population of PLWH continues to age, gaining a deeper understanding of the immune factors that drive acute neuroinflammation and contribute to persistent chronic neuroinflammation during ART become increasingly vital.

Originally identified as the AIDS dementia complex, HIV-associated neurocognitive disorders (HAND) or Neuro-HIV encompass a range of neurologic complications varying from mild to severe cognitive and motor impairments [13-15]. While severe forms of Neuro-HIV are less prevalent today, HIV infection continues to impact the brain, leading to HAND or HIV-associated brain injury (HABI) [16]. It is hypothesized that early HIV entry into the central nervous system (CNS) causes lasting effects on the brain, termed legacy HABI, even with suppressive ART. Additionally, as the infection progresses, active HABI contributes to a gradual cognitive decline. The role of immune activation in driving neuroinflammation in Neuro-HIV is crucial, but the specific cellular mediators responsible for both neuroinflammation and viral persistence in the CNS during chronic infection, as well as immune activation prior to ART initiation, are not yet fully understood.

The historical identification of multinucleated giant cells in brain parenchyma and encephalitic lesions, along with the association of HIV-1 with brain parenchymal macrophages in AIDS patients, brought focus to brain-resident myeloid cells as crucial drivers of viral persistence and neuroinflammation [17, 18]. Observations of CNS compartmentalized viral variants, assessed by viral genomic sequencing within the cerebrospinal fluid (CSF) showed ability to mediate infection of cells with lower levels of CD4, and longer half-lives post-acute infection. These data indicated that long-lived cells such as brain-resident macrophages and microglia gradually replace CD4 T cells as the primary source of the virus in the CNS during the chronic phases of infection [19, 20]. To reproduce these outcomes, studies in non-human primate models utilized macrophage tropic viral clones that do not depend on high CD4 receptor expression for entry. Additionally, accelerated experimental models intended to increase the frequency, severity, and kinetics of CNS disease in NHP employed CD8 depletion strategies in combination with R5-T cell tropic viruses to induce an immunosuppressive state, leading to the frequent, early development of classic encephalitis lesions typically observed in end-stage Neuro-HIV [21-25]. These accelerated models have contributed to our understanding of how HIV establishes itself in the brain during early infection and quickly multiplies within the CNS during profound immune dysfunction. However, it is essential to note that they do not offer insights into CNS dissemination during most natural transmissions.

To understand the neuroinflammatory triggers leading to neurodegeneration in the modern ART era, it is crucial to leverage our enhanced understanding of CNS immune surveillance to explore viral dissemination in multiple immune-rich niches of the CNS during both acute infection and suppressive ART. To achieve our research objectives, we utilized two macaque cohorts. The first cohort consisted of macaques acutely infected with SIVmac251, and they received no ART. The second cohort was infected with SIVmac251 and assessed up to week 42 post infection. We initiated ART at week 3 and therapy was periodically interrupted to simulate suboptimal

adherence, referred to as deferred non-adherent ART regimen. We aimed to characterize the viral-immune interactions involved in establishment and persistence of SIV infection in the CNS. Our findings support three major conclusions. Firstly, we observed that antigen-experienced CD4 T cells present within the brain parenchyma, choroid plexus stroma, dura mater, skull bone marrow, and CSF exhibit a distinctive profile expressing either CCR5 or CCR7. During acute infection, we observed high tissue viral loads within the frontal and temporal lobes, as well as in border tissues, including the lymphoid niche of the skull bone marrow. Associated CD4 T cell depletion within these compartments was suggestive of ongoing CD4 T cell infection in the CNS which was not rescued following suppressive ART. Notably, the relative distribution of CCR5 and CCR7 subsets remained stable throughout this process. Secondly, we found that during ART, CSF viral RNA (vRNA) was below the limit of detection (<15 vRNA copies/ml CSF) despite persistent low vRNA levels in the brain, underscoring the intricate nature of viral control in the CNS. Thirdly, we document a previously unknown potential HIV reservoir in the skull bone marrow. Together, our studies provide insights into the interplay between viral dissemination, CNS T lymphocytes, and neuroinflammation, critical to inform the development of targeted approaches to mitigate progressive neurodegeneration in the context of modern ART.

## RESULTS

### Study Design

To understand HIV-1 CNS involvement during both the acute and chronic phases of infection, we conducted studies using two macaque cohorts. We employed CCR5-tropic SIVmac251 to replicate acute and chronic HIV-1 effects on the CNS during natural transmission. The first cohort, known as the Acute 251 cohort, comprised four macaques assessed at week 3 pi (SIV,w3). The second cohort, referred to as the Chronic 251 cohort (n=6), was followed for a duration of up to 40 weeks post-infection (pi). Throughout the study, we collected plasma and CSF samples to capture viral and immune kinetics in both the systemic and the CNS compartments. Four uninfected age-matched animals served as controls. At necropsy, tissues were collected following trans-cardiac saline perfusion to ensure that the assessment of immune cells in the CNS compartment reflected CNS tissues without contributions from vasculature contents. Comprehensive details of the animals can be found in **S1 Table**.

To capture early-stage dynamics in the CNS prior to ART initiation, we utilized the Acute 251 cohort (**Figure 1A**). In this study, we utilized both flow cytometry analysis of CNS immune cells and single-cell RNA sequencing on CD45+ cells extracted from the brain. This comprehensive approach allowed us to gain deeper insights into the acute neuroinflammatory programs initiated in CNS CD4 T cells during this critical stage. We collected post-mortem punch biopsies of the brain parenchyma, immediately after the brain was excised, for viral quantification. The remainder of the right hemisphere was collected in media and processed immediately post-harvest to extract single cell suspensions for flow cytometry analysis.

In the Chronic 251 cohort (**Figure 1B**), our objective was to induce cycles of viral suppression and rebound throughout the course of infection, resembling scenarios of intermittent poor adherence to medication or drug resistance, as observed in real-life chronic HIV infections. To

achieve this, we employed a 3-drug ART regimen comprising of nucleoside/nucleotide reverse transcriptase inhibitors (NRTIs) Emtricitabine (FTC), Tenofovir (TFV) and the integrase inhibitor Dolutegravir (DTG), which was initiated at week 3 post-SIV inoculation, after peak viremia. In clinical studies, FTC and DTG attain therapeutic concentrations within the CNS [26, 27], while TFV's limited CSF diffusion, estimated at only 5%, leads to lower CNS penetration effectiveness scores[28, 29]. As CSF escape is an indicator of resistance, longitudinal assessment of paired plasma and CSF viral loads was performed.

Treatment interruption was initiated when CSF viral (v) RNA dropped below 100 copies/mL at two consecutive time points, accompanied by plasma viral loads below 10,000 copies/mL. Subsequently, ART was re-initiated when CSF vRNA exceeded 1000 copies/mL at a single time point. These repeated cycles of treatment interruption and initiation continued throughout the chronic phase of infection. Two-to-four weeks prior to necropsy, all SIV-infected animals received ART, and levels of antiretroviral drugs in the plasma, CSF, prefrontal cortex (PFC), and colon were quantified.

**CNS viral dissemination and neuroinflammation linked to decline in CSF CCR5+ CD4 T cells.**

In line with observations in humans [30, 31], we identified that the non-inflamed CSF allows entry of CD4 T cells, typified by an antigen-experienced CD28+ CD95+ phenotype. Notably, we identified the presence of a distinct CCR5+CCR7- subset, comprising approximately 34% (median) of antigen-experienced CD4 T cells in the CSF (range: 15-46%) in contrast to only 4% observed in blood and lymph nodes (**Figure 1C)**. The CCR5+ CCR7- subset of CD8 T cells exhibited higher prevalence in the blood (median 26%). Interestingly, like their CD4 counterparts, these frequencies were even more elevated in the CSF (median 76%, **S1A Fig**). On the other

208 hand, CCR7+CCR5- CD4 T cells were most prevalent in the blood, constituting 73% (range: 58-
209 75%), whereas they accounted for 58% in the CSF (range: 43-75%).
210
211 Based on the presence in the CSF of CCR5+ CCR7- CD4 T cells, consistent with ongoing immune
212 surveillance, we posited that rapid influx of infected CD4 T cells into the CSF following systemic
213 viral replication would lead to acute CNS viral dissemination. Complete blood counts with
214 differential quantitation revealed an expected decrease in CD4 T cell counts (1.8-fold decline at
215 week 4 relative to week 0, $p < 0.05$) with no significant change in total lymphocyte counts during
216 acute infection (**S1B-C Fig**). During the initial week post-infection, the median levels of CSF vRNA
217 were approximately 31,000 copies. By the second week, CSF vRNA reached a peak of 1.7x10^6
218 copies before gradually declining to 2.65x10^5 copies by the third week. These observed patterns
219 closely paralleled viral kinetics in plasma, albeit at lower levels (**Figure 1D-E)**.
220
221 Measurement of levels of interleukin 8, monocyte chemotactic protein (MCP-1) and interferon
222 protein 10 (IP-10) demonstrated significant induction of MCP-1 and IP-10 in plasma, peaking at
223 week 1 and gradually declining afterward, while remaining significantly higher than baseline levels
224 at week 3 (**Figure 1F, S2 Fig**). In contrast to plasma levels, CSF MCP-1 concentrations did not
225 change significantly, and CSF IP-10 levels displayed a distinct pattern, continuously increasing
226 over time (**Figure 1G**). At week 2, CSF IP-10 levels showed a strong correlation with plasma IP-
227 10 levels, indicating that either CSF IP-10 was influenced by systemic induction or that intrathecal
228 IP-10 production occurred at a similar level as systemic IP-10 induction (**Figure 1H**).
229
230 Despite high viral loads, CD28+ CD95+ cells constituted the majority of CD4 T cells in the CSF
231 during acute infection (**Figure 1I**). At week 3, a notable decrease in the proportion of T cells in
232 the CSF was observed (**Figure 1J**), primarily driven by a sharp decline in CD4 T cell frequencies
233 during weeks 2 and 3 (**Figure 1K**) and influx of Gag-specific CD8 T cells (data not shown).

Remarkably, although IP-10 levels, which promote $T_h1$ cell ingress, were elevated, the proportion of CCR5+ CD4 T cells in the CSF declined. However, the CCR5+ CD8 T cell and CCR7+ CD4 T cell subsets remained relatively stable, suggesting the decline was specific to viral replication in target cells within the CSF (**S3 Fig**). As a result, a significant decrease in CD4:CD8 ratio in both CSF and blood ensued (**Figure 1L**). Viral suppression following ART initiation at week 3 led to significant CD4 T cell rebound both in systemic and CSF compartments (both $p < 0.05$) with expected reconstitution of CCR5+ CD4 T cells (**Figure 1M-N**). The decrease in CD4 T cells during viral replication and rebound following viral suppression supports local viral replication as a contributor to CSF viral loads. This interpretation is supported by evidence in macaques and humans of CD4-cell associated spliced vRNA within CSF indicative of active CD4 infection [32], although it does not rule out a potential contribution of virions transiting to the CSF from other sites of origin to total CSF vRNA levels [32].

Assessment of CSF albumin, total protein, and glucose levels indicated that the blood-brain barrier (BBB) maintained its functional integrity despite ongoing viral replication and neuroinflammatory response (**S4 Fig**).

**CCR5+ CD4 $T_h1$ cells populate brain parenchyma.**

Prior to delving into the effects of infection on brain T cell responses, we elucidated the distribution of CD4 T cells within the non-inflamed CNS of SIV-uninfected macaques. The tissues we analyzed included the brain parenchyma and its border-associated compartments, such as the choroid plexus stroma (ChP). The ChP plays a crucial role as the interface between the circulation and the CSF. Additionally, we studied the dura mater (dura), which represents the outermost meningeal layer and supports the meningeal lymphatics. Another important compartment we examined was the skull bone marrow (Sk BM), allowing us to assess the lymphoid niche of the

calvaria [33-35]. To complement our investigation, we also included the draining lymph nodes of the brain, the deep cervical lymph nodes (dCLN) and the ileum as a non-CNS tissue.

As shown in **Figure 2A**, flow cytometry analysis of single cell suspensions obtained from saline-perfused CNS tissues from SIV-unexposed control macaques highlighted a robust immune environment rich in T cells, with clear identification of distinct subsets of both CD4 and CD8 T cells (**Figure 2B**). To delineate CD4 T cell helper profiles in the CNS, we examined the brain, Sk BM, and spleen for expression patterns of CCR5 in the context of CCR6, a marker for $T_h17$ cells and CXCR3, the canonical $T_h1$ marker. Our analysis revealed that CD4 T cells expressed minimal amounts of CCR6 but were predominantly CXCR3+, consistent with CXCR3-mediated ingress of T cells to the CNS. Among CXCR3+ CD4 $T_h1$ cells, the expression of CCR5 was found to be approximately 47% in the brain, 40% in SkBM, and 14% in the spleen. This indicates that a significant proportion of $T_h1$ cells in the brain and SkBM could potentially be susceptible to R5-tropic infection through CCR5-mediated mechanisms (**Figure 2C, S5A-B Fig**). The assessment of integrin heterodimers $\alpha_4\beta_7$ and $\alpha_4\beta_1$, along with CCR5 co-expression on $T_h1$ cells in the CNS, revealed that the majority of CXCR3+ cells in the CNS were $\alpha_4\beta_1$+. The next most abundant subset was $\alpha_4\beta_1^+$ $CCR5^+$ cells; thus, $T_h1$ cells in the CNS co-expressed both $\alpha_4\beta_1$ and CCR5. A similar pattern of expression was also observed within the spleen(**Figure 2D**).

The distinct patterns observed in the CSF for CCR5 and CCR7 were similarly observed within the brain parenchyma and other CNS tissues (**Figure 2E**). However, the frequencies of CCR7+ CD4 T cells were lower in the brain compared to the CSF (**Figure 2F**). Furthermore, when we assessed the polyfunctionality of CD4 T cells, specifically their production of cytokines TNFα, IFNγ, and IL-2 after stimulation with PMA/ionomycin, we discovered that CD4 T cells in the brain exhibited robust cytokine production (**Figure 2G**). The significant preponderance of IFNγ single-positive cells in the brain, of the parent CD95+ CD4 T cell population, compared to the spleen aligns with

the phenotypic data unequivocally demonstrating that $T_h1$ cells in the brain are highly functional much like their lymphoid counterparts(**Figure 2H**).

**CD4 T cells depleted in CNS tissues during acute SIV infection.**

Next, we studied the Acute cohort and investigated the impact on CD4 T cells in different CNS compartments during the acute phase of infection. Our analysis of all examined CNS tissues revealed a notable decrease in the relative proportion of CD4 T cells, accompanied by a corresponding increase in CD8 T cells compared to uninfected control animals (**Figure 3A**).

Upon assessing CD4 T cell phenotypes within the SIV-infected brain, we observed a modest, albeit statistically insignificant, increase in CD28- CD95 effector cells compared to the predominant CD28+ CD95+ subset (**S5C-D Fig**). Both CD28+ and CD28- CD4 T cell subsets exhibited heterogeneity for molecules such as CCR7, CD49d (α4 integrin), CXCR3, CD69, PD-1, and CCR5. However, a notable distinction emerged concerning CCR7 expression; CD28- cells were predominantly CCR7-, while the CD28+ subset showed heterogenous CCR7 expression. Despite the differences in CCR7 expression, both CD28- and CD28+ CD4 T cell subsets were present in similar proportions within the CNS during acute SIV, suggesting that both subsets were equally susceptible to viral-mediated perturbations within the CNS microenvironment.

During acute SIV infection, the brain and border tissues (dura and Sk BM) displayed distinct phenotypic distributions of CCR5+ and CCR7+ CD4 T cell populations, similar to the distribution seen in the non-inflamed brain during homeostasis. Notably, the CCR5+ CD4 T cell subset exhibited higher expression levels of CD69, PD-1, and CXCR3, indicating an activated and effector-like phenotype, while the CCR7+ CD4 T cells showed a quiescent phenotype, suggestive of a more resting state (**S5E-F**). In the CNS tissues, both CCR5 and CCR7 subsets of CD4 T cells were present at varying frequencies. The brain predominantly had CCR5 CD4 T cells, whereas

the spinal cord and Sk BM showed enrichment of CCR7 CD4 T cells, resembling the distribution observed in bone marrow of long bones and lymphoid tissues (**Figure 3C**).

To investigate the relationship between CCR5 and CCR7 expression during acute SIV infection, we examined the relative co-expression of two markers - PD-1, which indicates TCR stimulation, and CD69, a marker for acute activation and tissue residency. By analyzing t-SNE plots gated on CD4 CD95 T cells expressing a combination of either CCR5, CCR7, CD69, PD-1, we found that the majority of PD-1 and CD69 expression occurred within the CCR5-expressing CD4 T cells (**Figure 3D**). Relative distribution of these subsets demonstrated that cells co-expressing CCR5 CD69 and PD-1, as well as CCR5 and CD69, were most abundant in the brain and comparable to frequencies in dura (**Figure 3E-F**), relative to other compartments. Conversely, cells expressing CCR7 but neither of the other three markers (CCR7 single positive, SP) were significantly higher in the lymphoid tissues, as expected, relative to the brain. Altogether, the data show distinct compartmentalization of CCR5+ and CCR7+ CD4 T cells and reveal that despite CD4 T cell depletion within the brain parenchyma, both CCR5 and CCR7 subsets co-exist during acute infection.

**T Cell clusters within SIV-Infected Brain.**

To gain deeper insights into the inflammatory programs induced within T cells within the brain following SIV infection, we conducted single-cell transcriptomic profiling of CD45+ cells extracted from the brain of the Acute cohort. This analysis included 4 samples from acute SIV-infected macaques and 2 uninfected controls (**Figure 4A**). For the uninfected control samples, we observed a median of 115,884 mean reads per cell, with a median of 29,278 total genes detected. The SIV-infected brain samples exhibited 107,659 reads per cell and 29,541 identified genes. Upon performing cluster analysis on the SIV-infected brain samples, we identified six distinct

338 immune clusters, with all clusters except the dendritic cell (DC) cluster being shared with the
339 controls (**Figure 4B**).
340
341 To characterize these cell clusters further, we analyzed highly expressed genes within clusters
342 across all animals. The CD8 $T_{CM}$ cluster demonstrated significant expression of transcription
343 factors ID2 and JUN, among others (**Figure 4C**). In contrast, the CD8 $T_{EM}$ cluster exhibited
344 transcription factor ZEB2 and STA4, along with activation markers, CD69, and Ki67 [36]. The CD4
345 $T_{CM}$ cluster displayed expression of canonical genes CD28 and IL7R, while the
346 monocyte/macrophage cluster showed FC receptor and Class II gene expression. The NK cell
347 cluster was marked by the expression of killer cell lectin-like receptor (KLR) genes [37]. Notably,
348 the DC cluster was unique to the SIV condition and showed distinct expression of the canonical
349 myeloid transcription factor IRF8, as well as genes regulating antigen presentation, including
350 CD74 [38].
351
352 We aimed to identify viral transcripts within individual cells and their correlation with CD4 T cell
353 immune clusters. To quantify viral transcripts, we developed a custom reference by integrating
354 the SIV isolate SIVmac251.RD.tf5 (SIVmac251) data with the *M. mulatta* (Mmul_10) genome files.
355 With our customized reference successfully established, the resulting count matrix, including viral
356 transcripts, guided subsequent analyses. After validating the approach's effectiveness (signal
357 detected in SIV Brain immune clusters but not in controls Figure 4D-E, Controls), we merged CD4
358 and monocyte clusters where we observed co-localization of transcripts. The combined UMAP,
359 with overlayed SIVmac251 reference sequence, highlighted mapped reads associated with CD4
360 T cell clusters and, to a certain extent, monocyte/macrophage clusters in the brain **(Figure 4D).**
361 Notably, the CD4 cluster exhibited the highest expression of viral transcripts. Examination of
362 splenic CD45+ cells exhibited a similar viral transcript distribution pattern (**Figure 4E**).
363 Microscopic analysis of the prefrontal cortex (PFC) using RNAscope confirmed our PCR data,

364 revealing the co-localization of viral RNA (vRNA) with CD3+ cells in the CNS parenchyma **(Figure**
365 **4F)**. During acute infection, SIV+ CD3+ T cells were observed in both perivascular and
366 parenchymal regions of the brain, particularly in the frontal cortex and hippocampus (Hp). This
367 collective information illuminates the pivotal role of CD4 T cells in facilitating viral dissemination
368 within the brain during SIV infection.
369
370 **T Cell Effector Molecular Programs Induced within the SIV-Infected Brain**
371 Upon comparing each immune cluster between SIV-infected brain samples and controls (**S6 Fig**)
372 and focusing on genes differentially up or downregulated with adjusted p values of $< 0.05$, we
373 noted the induction of a transcriptional program regulated by interferons, viral infection, and
374 pattern recognition receptors across all clusters (**Figure 5A**). The observed transcriptional
375 program encompassed several key components, such as interferon alpha inducible protein 27
376 (IFI27, up 8.8-fold, CD4 $T_{CM}$; 6.4-fold, CD8 $T_{CM}$; 7.8-fold, CD8 $T_{EM}$; 13.7-fold, Mono/Mac; 21-fold,
377 NK), IFI16 (5.1-fold, CD4 $T_{CM}$; 3.4-fold CD8 $T_{CM}$; 4.4-fold, CD8 $T_{EM}$; 8.5-fold, Mono/Mac; 9.7-fold,
378 NK); interferon stimulated genes which induce transcription of antiviral factors - ISG15 (2.8-fold
379 CD4 $T_{CM}$; 2.1-fold CD8 $T_{CM}$; 2.6-fold, CD8 $T_{EM}$; 3.6-fold, Mono/Mac; 4.2-fold, NK) and ISG20 (1.6-
380 fold, Mono/Mac [39], and interferon induced protein with tetratricopeptide repeats which mediate
381 molecular signaling by forming complexes with cellular and viral proteins IFIT2 (1.6-fold,
382 Mono/Mac), IFIT3 (1.6-fold, Mono/Mac [40]. Also induced were the MX Dynamin like GTPases 1
383 and 2 (MX1 (1.8-fold, CD4 $T_{CM}$; 1.4-fold, CD8 $T_{CM}$; 3.3-fold, Mono/Mac; 2.3-fold, NK), MX2 (2.4-
384 fold, Mono/Mac; 1.5-fold, NK). Notably, within the monocyte/macrophage cluster the cytidine
385 deaminase targeting primate lentiviruses, apolipoprotein B mRNA editing enzyme catalytic
386 subunit 3A (APOBEC3A), was induced 3-fold [41].
387
388 The pattern of antiviral gene expression closely resembled that observed for CD4 and
389 monocyte/macrophage clusters in the spleen, suggesting that CD4 T cells in both compartments

exhibited similar biological responses to viral infection (**Figure 5B**). Within CD4 $T_{CM}$ cluster, genes representing pathways regulating antiviral response, cytolytic function, defense response, metabolism were highly enriched (**Figure 5C**).

Based on induction of genes related to T cell activation and differentiation (CCL5, LAG3, ZEB2) and cytolytic function (GZMM, NKG7), and the downregulation of IL7R in the $T_{CM}$ cluster within the SIV brain, we hypothesized that the observed changes in gene expression patterns reflected a spectrum of T cell differentiation states. To test this hypothesis, we utilized an unbiased pseudotime approach where we identified four distinct lineages (**S7 Fig**), each characterized by unique gene expression profiles. Among these lineages, two lineages stood out due to expression of genes representing transition of $T_{CM}$ to $T_{EM}$ states (**Figure 5D-E, S7B-C Fig**). Along this trajectory was induction of genes associated with cell cycle progression (TK1, MKI67, EIF1, S100A10, S100A4), immune cell activation and differentiation (ZEB2, KLF2, CD52) [42], cytotoxic function (PFN1, GZMB, GZMH, NKG7, and CST7) [43]. Modest upregulation of genes from the ribosomal family, involved in regulating translation was also observed. In contrast, canonical $T_{CM}$ genes, such as IL7R and LTB, were downregulated in this lineage, suggesting a distinct pattern of gene expression associated with the differentiation process induced by SIV infection.

Collectively, the data revealed induction of an antiviral transcriptional program across all immune clusters, underscoring the robustness of the immune response; each cluster exhibited unique inflammatory pathways tailored to complement the specialized antiviral functions of individual immune subsets.

**vRNA in brain regions controlling cognitive function and within CNS border tissues.**

The sc RNA seq data and flow cytometry data demonstrating co-existence of activated CCR5+ CCR7- CD4 T cells alongside quiescent CCR7+ CCR5- CD4 T cells in the Acute cohort raised

possibilities regarding their potential roles in viral replication. To delve into this hypothesis, we quantified cell-associated vRNA and vDNA levels within specific CNS tissues. We collected post-mortem punch biopsies (~30 mg) from specific regions of interest, including both white (w) and gray (g) matter regions of the PFC and temporal lobe, such as the superior temporal sulcus (STS). Additionally, we assessed other CNS regions, including the hippocampus (Hp), pituitary (pit), a circumventricular organ, as well as the border tissues (ChP, dura, Sk BM). The data revealed high levels of vRNA within the brain parenchyma, with a median of 0.23x10^5 vRNA copies per 10^6 cells (**Figure 6A**). The viral loads in the border tissues were also high, with the ChP exhibiting a median of 0.5x10^5 vRNA copies, the Dura 5x10^6 vRNA copies, and the SkBM with 0.6x10^5 vRNA copies, indicating widespread viral dissemination throughout the entire CNS.

Assessment of vDNA across these regions showed a median of 139 vDNA copies/$10^6$ total cell equivalents observed in the frontal and temporal lobes (**Figure 6B**). Viral DNA was prominently observed in border tissues, with the Dura showing the highest levels of vDNA at 11,000 copies/$10^6$ total cell equivalents. The elevated viral burden in the dura aligns with its role in draining antigens from the CNS. The computation of the vRNA/vDNA ratio indicated active viral expression across all regions within CNS. Particularly noteworthy was the observation of higher ratios in white matter regions, known to harbor T cells [44] (**Figure 6C**). This observation aligns with imaging studies in PLWH, which have demonstrated widespread and rapid loss in white matter volume during the early stages of infection, while loss in gray matter is more defined and localized to specific regions of the parenchyma, such as the caudate nucleus [45, 46]. Collectively, the combination of phenotypic data, sc analysis, RNAscope, and viral load analysis indicates that the CNS is permissive to the replication of R5-T cell tropic viruses.

442 **Decrease in vRNA in Brain during Antiretroviral Therapy.**

443 To complement our data characterizing the establishment of CNS infection over the first 3 weeks
444 of infection in the Acute cohort, we turned to the Chronic cohort, in which we initiated ART at week
445 3 pi, we monitored CSF viral kinetics (**Figure 7A)**. The time taken to achieve viral suppression in
446 the CNS (defined as CSF vRNA copies at or below 15) varied between 3 to 7 weeks. During this
447 period, transient on ART increases in the CSF vRNA level occurred between 5 and 7 weeks in
448 some animals, except for one animal. Remarkably, 37274 Mamu A*01, demonstrated notable
449 CSF viral suppression even without the ART suggestive of SIV-specific CD8 T cell mediated viral
450 control in the CSF in this animal.
451
452 Initially, there was a rapid decay of CSF viremia up to week 6, which closely mirrored the decay
453 of plasma viral loads during ART. This observation suggests that viral output during the acute
454 phase was primarily due to viral replication in short-lived cells. Interestingly, a slower second
455 phase of decay was observed in 3 animals, indicating the potential involvement of long-lived cells
456 such as macrophages in viral persistence [19, 20, 47]. Subsequent suppressive periods showed
457 shorter intervals, consistent with lower initial CSF viral loads (median 5,150 vRNA copies/mL) and
458 rapid decay kinetics. Once cycles of ART withdrawal were initiated, plasma and CSF vRNA
459 rebound was observed for all animals, except for 37274 that achieved suppression of CSF vRNA
460 (but not plasma vRNA) while off ART.
461
462 To assess evidence of viral expression in the setting of ART suppression of viral replication, we
463 implemented a strategy where all animals were on ART for a period of 2-4 weeks before necropsy.
464 This intervention led to significant reduction of CSF vRNA levels to < 15 copies/mL. We also
465 evaluated the penetration of antiretroviral drugs (ARVs) into CSF. For this purpose, we quantified
466 ARV levels in both plasma and CSF samples obtained at the time of necropsy. To gain a deeper
467 understanding of ARV metabolism and intracellular levels of active metabolites, we also

468 investigated the presence of di and tri-phosphorylated forms of TFV/FTC within tissues. The
469 timing of sample collection was carefully coordinated to measure trough levels in plasma and CSF.
470 Specifically, samples were obtained 9-12 hours after the last ART dosage and were immediately
471 processed to preserve sample integrity. To examine tissue-specific effects, post-mortem punch
472 biopsies were collected from the PFC and colon, weighed, and flash-frozen for subsequent
473 analysis.
474
475 All three ARVs were measured, and the active metabolites of the NRTIs were quantified in colonic
476 (a site of peripheral viral replication) and PFC (a cognitive area of the brain affected in chronic
477 HIV) tissue. Consistent with previous studies [48], FTC exhibited the highest penetration, with
478 CSF levels similar to those observed in plasma (median ng/mL; plasma: 20.8; CSF: 12.5) (**Figure**
479 **7B)**. DTG was also found above the lower limit of quantification (LLOQ) in CSF for all animals
480 (median ng/mL; plasma: 329; CSF: 4.2, $p<0.05$). On the other hand, TFV showed detectable
481 levels in the CSF of only 2 out of 5 animals (median ng/mL; plasma: 58.8; CSF: 1.2, $p<0.05$). We
482 investigated the penetration of ARVs into brain tissue and observed that all ARVs were able to
483 penetrate the brain, with levels of TFV, FTC, and DTG above the LLOQ (**Figure 7C)**. However,
484 it's important to note that these levels were at least 10-fold lower compared to those observed in
485 colonic tissue. Importantly, we observed the accumulation of TFV di-phosphate (DP) in the PFC,
486 indicating the penetration of ARVs into the CNS (**Figure 7D)**.
487
488 Measurement of CSF viral loads demonstrated that vRNA levels were low to below threshold of
489 detection. In the gray matter of the PFC, measurable vRNA levels were observed in only 2 out of
490 6 animals, while all animals tested negative in the white matter of the PFC (**Figure 7E)**.
491 Interestingly, in the temporal lobe, there was a higher likelihood of focal viral expression, with
492 most animals showing vRNA in the STS and Hp. Within the border tissues, detectable vRNA in
493 the dura and Sk BM was found in all animals; however, vRNA in ChP in most animals was not

494 measurable, in line with concurrent CSF viral suppression. Evidence of viral infection was
495 observed with vDNA demonstrable across the brain parenchyma in all animals (**Figure 7F)**. These
496 collective findings strongly support the conclusion that lymphotropic viruses establish viral
497 reservoirs in the CNS. Having observed the active induction of IP-10 during acute viral infection
498 within the CNS, we further explored its potential as a biomarker for ongoing viral replication during
499 the chronic phase. Despite viral suppression, we observed a trend for higher IP-10 levels in CSF
500 relative to baseline and concurrent plasma levels (**S8 Fig)**.
501
502 **Persistent CD4 depletion in CNS during chronic infection**
503 The presence of vRNA in the brain parenchyma and associated border tissues during suppressive
504 ART led us to hypothesize that CD4 T cells would remain depleted in the CNS during chronic
505 infection. To explore this, we assessed CD4 T cell frequencies in various CNS compartments,
506 including blood, brain, choroid plexus, CSF, dura, Sk BM, and dCLN (**Figure 8A**). Our analysis
507 confirmed our hypothesis, revealing a significant reduction in CD4 T cell frequencies compared
508 to uninfected control animals (**Figure 8B**).
509
510 To further investigate the changes within CD4 T cell subsets during acute and chronic infection in
511 the brain parenchyma, we focused on $T_h1$ cells expressing $\alpha_4\beta_1$ and CCR5, comparing them to
512 relative differences observed in the spleen. The proportion of CXCR3+CCR5+ CD4 T cells
513 remained constant with infection, while there was a relative decline in these cells in the spleen
514 during the acute phase. Meanwhile, both $\alpha_4\beta_1$+ CD4 $T_h1$ and $\alpha_4\beta_1$+ CCR5+ $T_h1$ cells were
515 significantly reduced during acute infection in both the brain and spleen (**Figure 8C**).
516 During the chronic phase, subsets expressing either CCR5 or CCR7 were still observed (**Figure**
517 **8D**). t-SNE plots of CD4 CD95 T cells expressing CCR5/CCR7/CD69/PD-1 demonstrated a
518 distribution pattern similar to that observed during acute infection (**Figure 8E-F**). Notably, cells
519 expressing PD-1 but not CCR7, CD69, or CCR5 (PD-1 single positive (SP) were present at higher

frequencies during the chronic phase (**Figure 8G**). This increase in the relative frequencies of the PD-1 SP subset was also observed in the dCLN. Furthermore, while PD-1+ CD69+ CD4 T cells were not significantly higher in the brain during the chronic phase, their frequencies were elevated in the dura and dCLN. Additionally, an increase in the CCR7+ PD-1+ CD4 T cell subset was noted in the dura and dCLN. Overall, the data show that there is an increase in CD4 T cells expressing PD-1 within the brain parenchyma and CNS during the chronic phase of infection, even with suppressive ART. This increase indicates ongoing antigen-mediated T cell stimulation in CNS.

## DISCUSSION

A deeper understanding of immune mechanisms driving viral establishment, persistence and neuroinflammation holds the potential to improve the quality of life for those living with HIV by addressing neurological complications and cognitive impairments early and effectively. Our findings provide significant insights into the immune environment within the brain parenchyma during both acute and chronic HIV infection. Specifically, we have identified distinct subsets of activated CCR5+ CD4 T cells and resting CCR7+ CD4 T cells. This discovery, coupled with our existing knowledge of these cell subsets derived from lymphoid and mucosal tissues [49-52], strongly supports the hypothesis that the immune milieu in the brain facilitates both active viral replication and the persistence of viral reservoirs during R5-T cell tropic infections. Notably, our single-cell, phenotypic, and functional analyses demonstrate striking parallels between CD4 T cells in the brain parenchyma and those within the spleen during acute SIV infection. Beyond the brain parenchyma, our research sheds light on the immune composition of brain border tissues, uncovering HIVtarget CCR5+ CD4 T cells in the choroid plexus, dura, and skull bone marrow. The presence of vRNA and vDNA in these areas, along with their interconnectedness, holds significant implications. These findings indicate that CSF viral loads can provide more comprehensive insights than previously appreciated. They may not only reflect viral activity in the brain parenchyma and blood but also indicate viral presence in the choroid plexus and skull bone marrow. Equally notable is the existence of a lymphoid niche composed of CCR7+ cells expressing IL-7R in the CNS. This finding is important as homeostatic proliferation of these cells could contribute to the longevity of virally infected cells within the CNS. In summary, our work not only sheds light on the intricate CD4 T cell landscape within the CNS but also highlights the active responses of T cells to SIV infection. These findings hold the potential to guide the development of precisely targeted interventions against Neuro-HIV.

In addition to CD4 T cells, our single-cell analysis of CD45+ cells from the brain demonstrates the presence of distinct CD8 $T_{CM}$ and $T_{EM}$ clusters during acute SIV infection. While we did not identify a definitive resident memory ($T_{RM}$) cluster [53] the expression of CD69 transcripts within $T_{EM}$ and CD69 surface expression strongly suggests the co-existence of effector and resident CD8 T cells within the rhesus brain parenchyma. Furthermore, CD69 alone, in the absence of CD103, is shown to be sufficient in identifying $T_{RM}$ in non-CNS tissues [54]. This indicates that T cells in the brain exhibit a spectrum of differentiation states and respond rapidly to SIV infection in the CNS. Notably, we observed the upregulation of the canonical pathogen-specific effector chemokine, CCL5, in the CD8 $T_{EM}$ cluster. Additionally, the presence of Ki-67, a marker for cellular proliferation, is consistent with active recruitment of SIV-specific CD8 T cell effectors to the brain parenchyma during acute infection [55, 56]. Our single-cell analysis of the CD4 T cell cluster in the brain also uncovered crucial details into the immune response during acute SIV infection. We observed a significant downregulation of key genes, such as IL7R and CD4, indicating strong T cell activation. Additionally, the expression of important anti-inflammatory receptors, including ADORA2B (receptor for extracellular adenosine) and the glucocorticoid receptor NR3C1, was also reduced. Conversely, we also noted the activation of antiviral IFN genes, signifying the active engagement of CD4 T cells within the brain. Importantly, this antiviral gene expression pattern closely paralleled what was observed in CD4 clusters within the spleen, indicating a shared antigen-specific and bystander response pattern across infected tissues. Exploring clonal heterogeneity of T cell subsets will yield deeper insights into immune response dynamics within the CNS during infection.

Although we did not measure cell-associated vRNA in CD4 T cells in the CSF in our studies, we infer the contribution of productive CD4 infection to CSF viral burdens. This inference is supported by the fact that R5-T cell tropic viruses, such as SIVmac251, require high levels of CD4 to enter cells. Previous research has also shown rapid viral decay following ART initiation, which aligns

with our observations, consistent with replication in short-lived T cell effectors [47] [57]. Recent studies have shown spliced cell-associated viral RNA in CSF CD4 T cells during the acute stages of HIV-1 infection and weeks 2, 4, and 8 in SHIV-infected macaques, supporting active viral transcription within CSF CD4 T cells [32]. Studies in PLWH during suppressive ART further support this model [32, 58]. Utilizing the T cell activation marker CD26 to distinguish HIV virions derived from CD4 T cells versus macrophages, Lustig et al. report T cell-derived virus in the CSF, even in individuals experiencing CSF escape - controlled viral replication in periphery evidence by plasma viral loads below the limit of detection in presence of concurrent CSF viral loads [58]. Although compartmentalized virus in the CSF has been attributed to viral replication in brain-resident myeloid cells [20], compartmentalized replication of R5-T cell tropic T/F virus in ART-naive PLWH has also been observed [57]. Altogether these data support the importance of CD4 T cells in contributing to acute stage CNS viral burden and neuroinflammation, setting the stage for legacy effects.

The presence of HIV target CCR5+ CD4 $T_h1$ cells in immune-rich compartments within the CNS beyond the CSF highlights their potential role in supporting viral replication. Notably, higher levels of vRNA within the dura, compared to the parenchyma, might be attributed to transitory cells draining from the brain and subarachnoid space through dural lymphatic vessels, although the possibility of resident cells in this compartment cannot be ruled out [33, 59]. Another intriguing site is the choroid plexus stroma, positioned at the interface of peripheral blood and CSF, known to harbor macrophages and dendritic cells. The presence of CCR5+ CD4 T cells and vRNA in this location underscores its importance in terms of inflammation and viral evolution. Of particular significance is the potential establishment of reservoirs in the skull bone marrow niche of the CNS, which has access to the dura and brain, especially in the context of inflammation [60, 61]. Based on the mobilization of the myeloid niche from the skull bone marrow to the brain during inflammation [60], investigating whether a similar phenomenon occurs for T cells could yield

623 valuable insights into their migration and role in seeding the brain with virally reactivated CD4 T
624 cells. Furthermore, the homeostatic proliferation of CCR7+ cells and clonal expansion within the
625 marrow may contribute to reservoir maintenance, potentially enabling the transit of cell-free or
626 cell-associated virus to border tissues of the brain and the CSF. Assessing viral sequences in
627 sorted CCR5+ and CCR7+ subsets across CNS compartments and in peripheral subsets during
628 acute and chronic infection under suppressive ART will provide deeper insights into their
629 respective roles in promoting viral replication and persistence.
630
631 Our systematic investigation, encompassing evaluations of T cells across controls, as well as
632 during the acute and chronic stages of SIV infection, lend support to the hypothesis that a
633 continuous influx of CCR5+ CD4 T cells into the CNS throughout the course of HIV infection
634 sustains both viral persistence and neuroinflammation. This hypothesis is supported by the
635 following pieces of data. To begin, the strategic positioning of CXCR3+ CCR5+ CD4 T cells within
636 various CNS regions - including the brain parenchyma, CSF, choroid plexus stroma, dura, and
637 skull bone marrow - highlights their significance not only in neuroinflammation but also in
638 sustaining CNS viral presence. In support of this concept, consistent elevation of CSF IP-10 levels
639 compared to plasma throughout infection signifies a CNS environment primed for CXCR3-IP-10
640 mediated T cell ingress. This implies that the CNS remains receptive to CCR5+ CD4 T cell
641 infiltration, potentially perpetuating viral presence. Equally pivotal is data showing that despite
642 CD4 T cell depletion during infection, frequencies of CCR5 and CCR7 within the CNS remain
643 relatively stable. This stability prompts consideration that underlying mechanisms sustain a pool
644 of CCR5+ CD4 T cells within the CNS. The presence of CCR5+ CD4 T within the skull bone
645 marrow, coupled with activation of the skull bone marrow niche during neuroinflammation,
646 indicates possible conduit for cell-free or cell-associated viral migration from the skull bone
647 marrow to the brain [61]. By investigating dynamics of viral sequences across different CNS
648 compartments, future studies may uncover insights into CNS viral evolution and the role of CCR5+

649 CD4 T cells in driving this process.

650

651 Once inside the brain, T cell engagement with brain-resident innate immune cells can trigger
652 robust immune activation. Indeed, the consideration of brain resident microglia and macrophages
653 is paramount in understanding the full extent of viral dissemination and neuroinflammation within
654 the CNS. As major immune cells expressing CD4 and CCR5, albeit at lower levels than CD4+ T
655 cells, they become crucial targets for viral infection in the CNS [57, 62]. High responsiveness of
656 microglia to IFNγ, a classic CD4+ $T_h1$ cell cytokine, can activate them, leading to the release of
657 free radicals and inflammatory mediators like TNFα and IL-1β, ultimately contributing to neuronal
658 death [63-65]. This ensuing inflammation, particularly the induction of IP-10, could then trigger
659 waves of $T_h1$ CD4 T and CD8 T cell influx, further intensifying immune activation. Such a
660 continuous cycle of viral replication and immune activation could contribute to viral persistence
661 within the CNS. Conducting proof-of-principle studies to investigate these mechanisms and
662 delineating the role of immune trafficking across distinct CNS compartments is of utmost
663 importance as they hold the potential to significantly advance our understanding of the cells
664 involved in acute and chronic neuroinflammation, as well as viral persistence within the CNS.

665

666 In conclusion, our findings provide insights into viral replication and immune responses within the
667 CNS. They have important implications for understanding disease progression, viral persistence,
668 and the challenges in eradicating the virus from the CNS.

669

670
671
672
673
674
675
676
677
678

679 **FIGURE LEGENDS**

680 **Figure 1. CNS viral dissemination and neuroinflammation linked to decline in CSF CCR5+**
681 **CD4 T cells.** Study design of (**A**) Acute 251 cohort and (**B**) Chronic 251 cohort. (**C**) Flow cytometry
682 plots illustrate discrete distribution patterns of CCR5 and CCR7 on CD4+ CD95+ cells in blood,
683 lymph node fine needle aspirate (FNA), and CSF in SIV unexposed controls. Bar graphs show
684 frequencies of CD4 subsets across compartments. Kinetics of viral RNA (copies/mL) measured
685 by RT-qPCR in (**D**) plasma and (**E**) CSF following SIVmac251 infection. Horizontal dashed line
686 indicates limit of detection (15 vRNA copies/ml). Concentrations of IP-10 (pg/mL) measured in **(F)**
687 plasma and **(G)** CSF by Legend Plex flow-cytometry based bead assay. **(H)** Bubble plot shows
688 correlation of CSF and plasma IP-10 at week 2 post SIVmac251, Spearman correlation, two-tailed
689 p value shown. Bubble size denotes CSF viral load (CSF VL), and bubble color intensity denotes
690 plasma viral load (PVL). **(I)** Flow cytometry plot illustrates CD4+ CD95+ T cells express CCR5
691 and CCR7 in CSF. **(J)** Kinetics of CSF T cells during acute SIV**. (K)** Kinetics of CD4+ T cells in
692 CSF; graphs show % CD4 T cells, %CCR5+ CD4 T cells and % CCR7+ CD4 T cells in CSF. **(L)**
693 CD4:CD8 Ratio in CSF and Blood. **(M)** Plasma viral loads following ART (week 3-7), CD4 T cell
694 rebound following viral suppression. **(N)** shows CSF vRNA during ART and CD4 T cell rebound
695 and reconstitution of CCR5+ CD4 T cells. Significant differences by two tailed Wilcoxon matched-
696 pairs signed rank test, ***, p< 0.01; **, 0< 0.01 in C. Significant differences by one tailed Mann
697 Whitney test ,*, p< 0.05 in F and G. Significant differences by one-tailed Wilcoxon matched-pairs
698 signed rank test ,*, p< 0.05 in J-N.
699
700 **Figure 2. CCR5+ CD4 $T_h$1 cells populate brain parenchyma. (A)** Flow cytometry plots illustrate
701 frequencies of CD4 and CD8 T cells in blood, CNS tissues, dCLN and ileum. **(B)** Contingency
702 plots show % CD4 (solid) and % CD8 (transparent) in each of the four control animals assessed.
703 **(C)** Surface expression of CCR6, CXCR3, and CCR5 on CD95+ CD4 T cells. Pie chart shows
704 preponderance of CXCR3+ CCR5+ (X3 R5) subset in brain relative to spleen. **(D)** Flow plots

andpie chart illustrate expression of $\alpha_4\beta_1$,$\alpha_4\beta_7$, and CCR5 on CD4 $T_h1$ cells. **(E)** CCR5 CCR7 distinction in CNS. **(F)** Contingency plots show % CCR5 (solid) and % CCR7 frequencies (transparent) in each of the four control animals assessed. **(G)** Flow plots show cytokine production following 3-hour stimulation with PMA/Ionomycin. **(H)** Pie Chart and bar graph show proportion of cytokine producing cells across brain and spleen. Significant differences by one tailed Mann Whitney test ,*, $p< 0.05$ in H.

**Figure 3. CD4 T cells depleted in CNS tissues during acute SIV infection. (A)** Bar graphs show T cell frequencies across blood, CNS tissues, dCLN, and ileum in control and SIV infected (week 3 pi) macaques**. (B)** Flow plots and **(C)** contingency plots show CCR5 / CCR7+ CD4 T cell subset frequencies at 3 weeks post SIV. **(D)** t-SNE plots gated on CD4+CD95+ cells in Brain expressing CCR7/CCR5/PD-1/CD69 (n=4 samples, 6390 events). **(E)** Pie chart demonstrating proportion of CD4 T cells expressing combination of markers (CCR7/CCR5/PD-1/CD69). **(F)** shows distribution of specific subsets across tissues. Significant differences by one tailed Mann Whitney test ,*, $p< 0.05$ in A and F.

**Figure 4. T Cell clusters within SIV-Infected Brain. (A)** Schematic of single cell profiling on CD45+ cells in brain. Sequence alignment to *M.mulatta* (Mmul_10) reference using 10X Genomics protocol (CellRanger V.6.0) was performed. The generated cell-by-gene count matrix was used for downstream analysis using the Seurat based integrative analysis workflow. The filtered count matrix (percentage of mitochondrial reads <10, and gene expressed in more than 10 cells) was log-normalized, with top variable genes used for graph-based cell clustering with a resolution of 0.5 and visualized using Uniform Manifold Approximation and Projection (UMAP). (**B)** UMAP of scRNA-seq transcriptional profiles from brain shows 6 clusters. Cell clusters are color-coded based on cell types. Cluster identity was assigned by a combination of approaches - cluster-specific differentially expressed genes, expert knowledge, canonical list of marker genes,

and automated annotations using immune reference atlas through SingleR. Inset shows cell proportions in each cluster by experimental group. **(C)** Dot plot of select marker genes expressed. Dot size represents proportion of cells expressing gene and color designates expression level. To quantify viral transcripts, we designed a custom reference using CellRanger mkref pipeline. We integrated FASTA and GTF files of SIVmac251 into *M. mulatta* (Mmul_10) genome references. This tailored reference facilitated downstream analysis by including viral transcripts in the count matrix. UMAP of SIV RNA expression in cell clusters (SIV RNA+ cell size increased for clarity) in **(D)** brain SIV counts, CD4 1276 cells; monocyte/macrophage, 516 cells, and **(E)** spleen SIV counts, CD4 1668 cells; monocyte/macrophage, 2312 cells. **(F)** shows SIV RNA in parenchyma and perivascular regions of the brain using ISH with probe against SIV Gag RNA. SIV RNA+ (green) CD3+ T cells (red) with nucleus (DAPI, blue) in PFC; boxes (CD3+ SIV+ cell); points to SIV+ CD3+ cells .

**Figure 5. T Cell Effector Molecular Programs Induced within the SIV-Infected Brain.** Differential gene expression (DEG) analysis of the different cell-types across conditions was performed using functions from Seurat; selection threshold of (adjusted p-value < 0.05, |log2 FC| > 0.25) based on Benjamini-Hochberg correction**. (A)** Heat map of DEG genes in controls (C) versus SIV for each immune cluster. **(B)** Venn diagram shows shared ISG upregulated post SIV across brain and spleen immune clusters. **(C)** Chord plot show pathways and corresponding genes enriched in SIV versus control CD4 $T_{CM}$ cell cluster in brain. We used the monocle3 based workflow to estimate the lineage differentiation between the cell population based on the experimental conditions. We extracted the subsets of the identified celltypes from our integrated Seurat object and further inferred the trajectory graphs. Using the defined root node (TCM), we chose the lineages based on the shortest path that connects the root node and the leaf node. After establishing different lineages, we implemented a differential gene test to find genes that

757 changed as a function of pseudotime based on a combination of Moran's statistic and q-value
758 and visualized using heatmaps and individual gene trajectory plots. **(D)** Heatmap shows changes
759 in gene expression in Lineage comprising of T cells. **(E)** shows expression levels genes of select
760 genes from heat map (ZEB2, LTB, GZMB) along pseudo-time.
761
762 **Figure 6. vRNA in brain regions controlling cognitive function and within CNS border**
763 **tissues. (A)** SIV vRNA (**B)** SIV vDNA (copies/10^6 cells) in brain regions specified (RT-qPCR on
764 post-mortem punch biopsies from specified regions. **(C)** shows vRNA/vDNA ratios.
765
766 **Figure 7. Decrease in vRNA in Brain during Antiretroviral Therapy.** Kinetics of plasma and
767 CSF viral suppression and rebound (vRNA copies/mL fluid, measured by RT-qPCR) over the
768 course of ART initiation and interruption. Green bars indicate periods of ART with FTC, TFV, and
769 DTG. Horizontal dashed line indicates limit of detection (15 vRNA copies/ml). **(B)** Concentration
770 of ARVs (ng/mL) in plasma and CSF quantified by LC-MS. **(C)** Concentration of ARVs (ng/mg) in
771 PFC and colonic tissue. (**D**) shows active phosphorylated forms of TFV and FTC. Spearman
772 correlation, two-tailed p value shown. Sampling was performed 2-4 weeks since ART initiation
773 with last ARV dose administered 9-12 hours prior to necropsy, FTC = emtricitabine,
774 TFV = tenofovir, DTG =dolutegravir, Gray shaded area represents lower limit of quantification of
775 assay. **(E)** SIV vRNA (**F)** SIV vDNA (copies/10^6 cells) in brain region (RT-qPCR on post-mortem
776 punch biopsies from specified regions. Gray shaded area represents viral loads below threshold
777 of detection. Significant differences by two tailed Wilcoxon matched-pairs signed rank test, * p<
778 0.05 in B-D
779
780 **Figure 8. Persistent CD4 depletion in CNS during chronic infection. (A)** Flow cytometry plots
781 illustrate frequencies of CD4 and CD8 T cells in blood, CNS tissues, and dCLN. **(B)** Bar graphs
782 show T cell frequencies across blood, CNS tissues, and dCLN in control and SIV infected

(chronic) macaques. **(C)** flow plots (top to bottom) show CD4 CD95 cells co-expressing CXCR3 and CCR5; $T_h1$ cells expressing $\alpha_4\beta_1$, and $\alpha_4\beta_1$ $T_h1$ cells expressing CCR5. Bar graphs show frequencies in brain and spleen and pie charts illustrate relative proportion of subsets in brain. (**D**) Contingency plots show distribution of CCR5 / CCR7 CD4 T cells in chronic SIV infection. **(E)** t-SNE plots gated on CD4+CD95+ cells expressing CCR7/CCR5/PD-1/CD69 (n=4 samples). **(F)** pie chart demonstrating proportion of CD4 T cells expressing combination of markers (CCR7/CCR5/PD-1/CD69). **(G)** shows distribution of specific subsets. Significant differences by one tailed Mann Whitney test ,*, $p< 0.05$.

809 **Data and materials availability**

810 RNA-seq dataset is accessible at **GSE221815**.

811

812 **Materials and Methods.**

813 **Ethics statement.** All animals were bred and housed at the California National Primate Research
814 Center (CNPRC) in accordance with the American Association for Accreditation of Laboratory
815 Animal Care (AAALAC) guidelines. All studies were approved by the University of California,
816 Davis Institutional Animal Care and Use Committee (IACUC).

817

818 **Rhesus macaques.** For Acute 251 studies, four (1 male and 3 females) colony-bred rhesus
819 Indian origin rhesus macaques (*Macaca mulatta*) were utilized. For the Chronic 251 study, six
820 adult (1 male and 5 females) Indian origin rhesus macaques (*Macaca mulatta*) were utilized. At
821 study initiation, animals were 11.2 – 17.4 years of age with a median weight of 10.5kg. Four
822 rhesus macaques served as controls (12-16 years, 1 male and 3 females). All animals were SIV
823 negative (SIV-), simian T-cell leukemia virus negative (STLV-), and simian retrovirus negative
824 (SRV-); and had no history of dietary, pharmacological, or surgical manipulation (***S1 Table***).

825

826 **SIVmac251 infection.** Rhesus macaques were infected intravenously with ($10^4$ TCID50)
827 SIVmac251 (2017 stock from CNPRC at 2.5 x 10^4 $TCID_{50}$/mL, grown in rhesus peripheral blood
828 mononuclear cells). Prior to inoculation, the virus was reconstituted in plain RPMI (virus stock:
829 RPMI ratio 4:1) in total injection volume of 500 µl.

830

831 **Antiretroviral therapy.** We formulated a triple-ART regimen described by Del Prete et al. [66]
832 containing the nucleo(s/t)ide reverse transcriptase inhibitors emtricitabine (FTC) and tenofovir
833 disoproxil fumarate (TDF) [from Gilead] with the integrase strand transfer inhibitor dolutegravir
834 (DTG) [from GSK].

**Viral RNA Quantification.** Quantification of plasma, CSF, and tissue viral RNA and viral DNA were performed essentially as previously described [67] with assays performed in the Quantitative Molecular Diagnostics Core of the AIDS and Cancer Virus Program at Leidos Biomedical Research Inc., Frederick National Laboratory.

**ARV measurement.** ARV concentrations in plasma, CSF, and tissue samples were quantified by LC/MS in the Clinical Pharmacology and Analytical Chemistry Core, UNC Center for AIDS Research as previously described [68].

**Specimen collection and processing.** Cerebrospinal fluid, blood, and lymph node fine needle aspirates were sampled and processed as described previously [69, 70]. For isolation of single cell suspensions from CNS compartments; tissues were mechanically dissociated and digested in DMEM with 0.25% trypsin and 5 units per mL of DNase I for 45 minutes at 37$^{o}$C. Digested tissues were homogenized using a pipette controller and 10mL serological pipette. The homogenized tissue was subsequently filtered through a metallic strainer followed by a 180µm nylon strainer and 100µm SMART strainer. Cells were washed in media and spun down at 1200 rpm for 10 minutes. Mononuclear cells were collected using a 21% and 75% Percoll gradient. Post gradient enrichment, cells were washed, counted, and up to 2x10^6 million cells were stained with panel of fluorophore conjugated antibodies or cryopreserved for future analysis.

**Flow Cytometry.** Whole blood, CSF, and fine needle lymph node aspirates (FNA) were freshly stained and acquired on the same day following collection. Mononuclear cells obtained from necropsy tissues were either freshly stained and acquired the same day or stained following cryopreservation. For cryopreserved cells, samples were thawed in ice baths and diluted in complete media. Cells were then washed and incubated in complete media with 2 units/mL of

DNAse I for 15 minutes at 37ºC. Cells were washed with complete media and counted prior to staining. Whole blood samples were treated with BD FACS Lysing Solution (BD Bioscience) for 10 minutes and washed with 1X FACS buffer (phosphate buffered saline with 1.5mM sodium azide, 2% fetal bovine serum, 10mM EDTA) prior to surface staining. Antibodies for surface staining were prepared in Brilliant Stain Buffer Plus (BD Biosciences) and incubated with cells at 4ºC for 30 minutes and washed twice with FACS buffer. Sample acquisition and fluorescence measurements were performed on a BD Bioscience FACSymphony utilizing FACSDiva software (Version: 8. 0.1). Sample compensation, population gating, and analysis was performed using FlowJo (Version 10.8.1)

**Legendplex assay.** This assay (BioLegend, USA) was conducted following the manufacturer's instructions to assess cytokine levels in plasma and CSF. Briefly, IP-10 (CXCL10, A6, cat# 740335), IL-8 (B7, cat#740344) and MCP-1(B9, cat#740345) multiplex beads were sonicated for two minutes in a sonicator bath (Thermo Fisher, USA). These multiplex beads were then appropriately diluted in assay buffer and added to a V-bottomed plate. Plasma samples were diluted 2-fold in dilution buffer, while CSF samples were used without further dilution. Both sample types were added to the V-bottomed plate containing multiplex beads and left to incubate overnight at 4°C on a microplate shaker at 150rpm. The next day, the plate was washed twice with washing buffer and 25µl of detection antibody was added to each well followed by washing and incubation for 1 hour on a microplate shaker at room temperature (RT). Then, 25µl of SA-PE was added into each well directly and incubated for 30 min at RT. The plate was washed twice and resuspended in 200µL of wash buffer. The samples were acquired on a BD LSR Fortessa (BD Biosciences, USA) cell analyzer, with 900 events collected from each sample for analysis. The concentration (pg/mL) of IP-10 (CXCL10), IL-8, and MCP-1 was determined by extrapolating the values from the standard curve.

887 **Cerebrospinal Fluid and Serum Biochemistries.** Animal CSF and serum chemistries were
888 quantified using a Piccolo Xpress Chemistry Analyzer (Abbott) with Piccolo BioChemistry Plus
889 disks in accordance with manufacturer's instructions. Chemistry panel analytes included albumin,
890 glucose, and total protein.
891
892 **Intracellular cytokine staining assay.** The polyfunctionality of CD4 T cells was assessed using
893 intracellular cytokine staining (ICS). Brain and spleen cells were stimulated with 1X Cell
894 Stimulation Cocktail (PMA and ionomycin) (eBioscience, USA) along with R10 media in the
895 presence of 0.2μg CD28/49d co-stimulatory antibodies (BD) per test. Unstimulated controls were
896 treated with volume-controlled DMSO (Sigma-Aldrich). Cells were incubated in 5% $CO_2$ at 37°C
897 and after 1 hour of stimulation, protein transport inhibitors 2μl/mL GolgiPlug (Brefeldin A) and
898 1.3μl/mL GolgiStop (Monensin) (BD, Biosciences, USA) was added to tubes and further incubated
899 for 3 hours at 37°C, 5% $CO_2$. Following stimulation, cells were stained for ICS surface markers
900 CD3, CD4, CD8, and CD95. Subsequently, the cells were fixed using cytofix/cytoperm for 10 min
901 at 4°C, then permeabilized with 1X Perm wash buffer (BD, Biosciences, USA), and stained with
902 intracellular markers TNFα, IFNγ, and IL-2 for 45 min. Finally, cells were washed and acquired
903 on the same day using a BD FACSymphony flow cytometer.
904
905 **Cell Preparation for Sequencing Studies.** Cryopreserved mononuclear cells from rhesus brain
906 were thawed at room temperature, placed in fresh complete media (For splenic cells: RPMI
907 supplemented with 10% HI-FBS, 1% L-glutamine, 1% penicillin-streptomycin; For brain tissue
908 derived cells: DMEM supplemented with 10% HI-FBS, 1% L-glutamine, 1% penicillin-
909 streptomycin) and treated with 2 units/mL of DNase I (Roche Diagnostics) for 15 minutes at 37ºC.
910 Cells were washed in complete media and CD45+ cells isolated using CD45 magnetic bead
911 separation for non-human primates (Miltenyi Biotec CD45 Microbeads non-human primate) in

accordance with the manufacturer's protocol. Enriched CD45+ cells were stained for CD45 and a live dead marker for subsequent flow cytometric sorting. Live CD45+ cells were characterized and quantified on a BD FACSymphony cell analyzer and sorted utilizing a FACS Aria and suspended in RPMI for single cell RNA sequencing studies.

**Single Cell RNA sequencing.** Sample barcoding, assembly of gel-beads in emulsion (GEM), GEM reverse transcription, cDNA amplification and cleanup, and library construction were performed according to the Chromium Next GEM single cell 3' v3.1 protocol from 10X Genomics. Sequencing was performed by SeqMatic LLC on a NovaSeq 6000 platform using S4 200 flow cells with paired end reads ran in four replicates with an average of 111,000 reads per cell. Sample demultiplexing, generation of FASTQ files, sequence alignment, gene counting, and sample aggregation were performed using the Cellranger pipeline version 7.1.0. Samples that passed data quality control steps (removal of samples with low quality reads, low frequency of mapped reads, low number of reads per cell, high mtRNA signature), were used for subsequent analyses. Sequenced reads were aligned to the Mmul_10 genome reference for Rhesus macaque, and raw count matrices were generated which were used as the input to the Seurat integrated analysis pipeline (Seurat V4.3.0). Quality control was done at the gene and cell level accounting for the median number of genes, and mitochondrial gene percentage using quality control plots.

**Bioinformatics.** To process the sequencing data, we performed sequence alignment to the reference genome of *M.mulatta* (Mmul_10) using the 10X Genomics protocol (CellRanger V.6.0). The generated cell-by-gene count matrix was used for downstream analysis using the Seurat based integrative analysis workflow. The filtered count matrix (percentage of mitochondrial reads <10, and gene expressed in more than 10 cells) was log-normalized, and the top variable genes were used to perform the graph-based cell clustering with a resolution of 0.5 and visualized using Uniform Manifold Approximation and Projection (UMAP). Cluster identity was assigned by a

combination of approaches which includes identifying cluster-specific differentially expressed genes, expert knowledge, canonical list of marker genes, and automated annotations using immune reference atlas through SingleR. Differential gene expression (DEG) analysis of the different cell-types across conditions was performed using the functions from Seurat and were selected at a threshold of (adjusted P-value < 0.05, |log2 FC| > 0.25) based on Benjamini-Hochberg correction. Gene-set enrichment analysis, and functional annotation was implemented through clusterProfiler 4.0, and visualized using custom scripts. All downstream data analysis was performed using R v4.2.0. We used the monocle3 based workflow to estimate lineage differentiation between the cell population based on the experimental conditions. We extracted the subsets of the identified celltypes from our integrated Seurat object and further inferred the trajectory graphs. Using the defined root node ($T_{CM}$), we selected lineages based on the shortest path that connects the root node and the leaf node. After establishing the different lineages, we implemented a differential gene test to find genes that change as a function of pseudotime based on a combination of Moran's statistic and q-value and visualized using heatmaps and individual gene trajectory plots. To count the viral transcripts in the data, we built a custom reference using the CellRanger mkref pipeline. We downloaded the FASTA and created the GTF files of Simian immunodeficiency virus isolate SIVmac251.RD.tf5 (SIVmac251) and added it to the reference genome files of *M.mulatta* (Mmul_10). The customized reference was successfully created, and the generated count matrix which includes the viral transcript was used in all steps of further downstream analysis. All downstream data analysis was performed using R v4.2.0. Venn diagrams were created utilizing http://bioinformatics.psb.ugent.be/webtools/Venn/

**In situ hybridization (ISH) and CD3 immuno-fluorescence.** In situ hybridization (ISH) and CD3 immuno-fluorescence were carried out following a modified version of the manufacturer's protocol (Document Number 322452-USM, 322360-USM, and UM323100, ACD) for RNAscope® ISH built on our previously established work [71]. The procedure involved several steps using the

964 RNAscope 2.5 HD brown Detection Kit and RNAscope® Multiplex Fluorescent Reagent Kit (ACD).
965 Initially, four-micron deparaffinized paraffin sections underwent pretreatment with 1X Target
966 Retrieval Buffer at 100°C for 15 minutes, followed by RNAscope Protease Plus at 40°C for 30
967 minutes before hybridization with probes at 40°C for 2 hours. Subsequent signal amplification
968 steps were conducted after hybridization. Detection of the signal was achieved using a DAB
969 solution for 10 minutes or TSA Vivid fluorophore 5 (Cat# 323271, ACD) for 10 minutes at room
970 temperature. For slides subjected to RNAsope alone, hematoxylin counterstaining was performed,
971 followed by dehydration, cover slipping, and visualization under bright-field microscopy using a
972 Zeiss Imager Z1 (Carl Zeiss). In cases where RNAscope was combined with CD3 immuno-
973 fluorescence, slides underwent an additional IHC staining process following RNAscope ISH. This
974 involved an overnight incubation at 4°C with Rat polyclonal anti-CD3 (Abcam) at a 1:100 dilution.
975 Detection of CD3 cells was facilitated by using Alexa Fluor 568 goat anti-rat IgG (Invitrogen). After
976 DAPI staining, slides were cover-slipped with ProLong Gold anti-fade mounting agent (Invitrogen).
977 In each ISH run, probe RNAscope Probe - SIVmac239 (Cat# 405661) was accompanied by
978 probes for dihydrodipicolinate reductase (dapB) or RNAscope 3-plex negative control probe.
979 Tissues from SIV-uninfected animals were also hybridized with the SIV probes to serve as
980 negative controls. To ensure the quality and consistency of the ISH assay, RNAscope® Probe -
981 Mau-Ppib and RNAscope 3-plex positive control probe were employed as positive controls for
982 RNA quality. Visualizations were carried out using appropriate filters, and images were captured
983 with a Zeiss LSM800 confocal microscope and Zeiss Imager Z2 (Carl Zeiss).
984
985 **Statistical Analyses.** Wilcoxon signed rank test were used for paired analyses (i.e., longitudinal
986 and within group comparisons). Mann-Whitney U-test were used for unpaired comparison
987 between animal cohorts/treatment groups. Test were performed in GraphPad Prism (Version
988 9.5.1) with significance values denoted as follows: * $p < 0.05$, ** $p < 0.01$, *** $p < 0.001$, **** $p <$
989 0.0001.

990 **Supporting Information**

991 **S1 Table.** Non-human primate cohort (Acute and Chronic 251 studies)

992 **S2 Table.** Antibody reagents for flowcytometry analysis.

993 **S1 Figure. CCR5/CCR7 dichotomy during homeostasis/Blood counts during acute**
994 **SIVmac251 infection. (A)** Bar graphs illustrate discrete distribution patterns of CCR5 and CCR7
995 on CD8+ CD95+ cells in blood, lymph node FNA, and CSF in SIV unexposed controls. **(B)** Kinetics
996 of body weight, white blood counts (WBC), red blood counts (RBC). **(C)** Kinetics of lymphocytes,
997 monocytes, and neutrophil counts during first 3 weeks of SIVmac251 infection in Chronic 251
998 cohort. Significant differences by Wilcoxon matched-pairs signed rank test, *, p< 0.05 **, 0< 0.01,
999 ***, p< 0.01.

1000 **S2 Figure. Plasma and CSF cytokines during acute SIVmac251 infection.** Kinetics of IL-8
1001 and MCP-1 measured by Legend plex assay during first 3 weeks of SIVmac251 infection in
1002 Chronic 251 cohort. Significant differences by Mann Whitney test *, p< 0.05.

1003 **S3 Figure. CSF CCR5+ CD8 T cell frequencies do not decrease during acute SIV infection.**
1004 shows % CD8 T cells, % CD28- CD95+ CD8 T cells, %CCR5+ CD8 T cells, and % CD69+ CD8
1005 T cells in CSF. Significant differences by one-tailed Wilcoxon matched-pairs signed rank test ,*,
1006 p< 0.05.

1007 **S4 Figure. CSF parameters during acute SIVmac251 infection.** CSF Albumin, protein, glucose,
1008 and glucose/albumin ratio during first 3 weeks of SIVmac251 infection in Chronic 251 cohort.

1009 **S5 Figure. CCR5+ CD4 T cells populate parenchymal and border CNS tissues. (A)** Flow plots
1010 and **(B)** bar graphs show CCR5 expression on CD4+CD95+ T cells in controls, second bar graph
1011 shows CCR5 CD8 frequencies. **(C)** Phenotypic characterization of CD28+ (blue) and CD28-(red)
1012 CD95+ cells in brain parenchyma and spleen. **(D)** shows distribution of CD28+ CD95+, CCR7+
1013 (% of CD28+ CD95+) and CD28- CD95+ CD4 (circle) and CD8 T cells (triangle) in brain
1014 parenchyma in controls (gray bars) versus SIV infected (red bars) macaques. **(E)** shows

phenotype of CCR5+ CCR7- versus CCR7+CCR5- cells. **(F)** bar graph of CCR5 /CCR7+ CD4 T cell subset frequencies in brain, dura, and skull bone marrow at 3 weeks post SIV.

**S6 Figure. Volcano plots of DEG in SIV brain.** Volcano plots of immune clusters show genes up and downregulated in SIV relative to controls. Genes meeting padj and fold-change cut-off are denoted in red.

**S7 Figure. Pseudo time plots of Control and SIV brain.** (**A**) UMAP. (**B**) pseudotime trajectory comprising of distinct immune clusters (**C**) shows heat map comprising of T cell clusters.

**S8 Figure. Kinetics of plasma and CSF vRNA, plasma IP-10 and CSF IP-10**. Green bar indicates duration of ART with FTC, TFV, and DTG. FTC = emtricitabine, TFV = tenofovir, DTG = dolutegravir.

**Acknowledgements**

The authors acknowledge several individuals whose contributions have been instrumental in the successful execution of the studies. The authors express their gratitude to Wilhelm Von Morgenland and Miles Christensen, as well as the CNPRC SAIDS team, for their coordination of macaque studies, animal care, and animal support. We also extend our appreciation to the CNPRC Veterinary Staff for their dedicated efforts in animal care and assistance. The authors are grateful to Yashavanth Shaan Lakshmanappa for his excellent technical assistance in preparation of ART, sample processing, and acquisition of flow cytometry data. The authors thank Chase Hawes, Jennifer Watanabe, and members of Koen Von Rompay's laboratory for valuable technical support during necropsies. We are thankful to Andradi Villabos for assistance provided during necropsies and for acquisition of flow cytometry data. The authors acknowledge funding support from NIAID, NIH K01OD023034 (SSI); NIA, RF1AG06001 (SSI, JHM); NIAID, NIH R56AI150409 (SSI) and support with federal funds from the National Cancer Institute, National Institutes of Health under contract number HHSN261201500003I and NCI contract 75N91019D00024 (JDL).

## Author Contributions

**Conceptualization**: John. H. Morrison, Smita. S. Iyer.

**Data curation**: Sonny R Elizaldi, Anil Verma, Zhong-Min Ma, Dhivyaa, Rajasundaram, Mackenzie L. Cottrell, Smita. S. Iyer.

**Formal analysis**: Anil Verma, Dhivyaa Rajasundaram, Jeffrey D. Lifson, Smita. S. Iyer.

**Funding acquisition**: John. H. Morrison, Smita. S. Iyer.

**Investigation**: Sonny R Elizaldi, Anil Verma, Zhong-Min Ma, Sean Ott, Dhivyaa Rajasundaram, Mackenzie L. Cottrell, Zandrea Ambrose, Jeffrey D. Lifson, Smita S. Iyer

**Methodology**: Sonny R Elizaldi, Anil Verma, Zhong-Min Ma, Sean Ott, Dhivyaa Rajasundaram, Mackenzie L. Cottrell, Jeffrey D. Lifson, John. H. Morrison, Smita S. Iyer.

**Project administration**: John. H. Morrison, Smita. S. Iyer.

**Resources**: Angela D. M. Kashuba, Jeffrey D. Lifson, John. H. Morrison, Smita. S. Iyer.

**Supervision**: Angela D. M. Kashuba, Jeffrey D. Lifson, John. H. Morrison, Smita. S. Iyer

**Writing** – original draft: Smita. S. Iyer

**Writing** – review & editing: Sonny R Elizaldi, Anil Verma, Zandrea Ambrose, Jeffery D. Lifson,

## References

1. Survival of HIV-positive patients starting antiretroviral therapy between 1996 and 2013: a collaborative analysis of cohort studies. Lancet HIV. 2017;4(8):e349-e56. Epub 2017/05/16. doi: 10.1016/s2352-3018(17)30066-8. PubMed PMID: 28501495; PubMed Central PMCID: PMCPMC5555438.
2. Teeraananchai S, Kerr SJ, Amin J, Ruxrungtham K, Law MG. Life expectancy of HIV-positive people after starting combination antiretroviral therapy: a meta-analysis. HIV Med. 2017;18(4):256-66. Epub 2016/09/01. doi: 10.1111/hiv.12421. PubMed PMID: 27578404.
3. Trickey A, Sabin CA, Burkholder G, Crane H, d'Arminio Monforte A, Egger M, et al. Life expectancy after 2015 of adults with HIV on long-term antiretroviral therapy in Europe and North America: a collaborative analysis of cohort studies. Lancet HIV. 2023;10(5):e295-e307. Epub 2023/03/24. doi: 10.1016/s2352-3018(23)00028-0. PubMed PMID: 36958365; PubMed Central PMCID: PMCPMC10288029.
4. van Sighem AI, Gras LA, Reiss P, Brinkman K, de Wolf F, study Anoc. Life expectancy of recently diagnosed asymptomatic HIV-infected patients approaches that of uninfected individuals. AIDS. 2010;24(10):1527-35. Epub 2010/05/15. doi: 10.1097/QAD.0b013e32833a3946. PubMed PMID: 20467289.
5. Larsen A, Cheyip M, Tesfay A, Vranken P, Fomundam H, Wutoh A, et al. Timing and Predictors of Initiation on Antiretroviral Therapy Among Newly-Diagnosed HIV-Infected Persons in South Africa. AIDS Behav. 2019;23(2):375-85. Epub 2018/07/17. doi: 10.1007/s10461-018-2222-2. PubMed PMID: 30008050; PubMed Central PMCID: PMCPMC6331268.
6. Nicolau V, Cortes R, Lopes M, Virgolino A, Santos O, Martins A, et al. HIV Infection: Time from Diagnosis to Initiation of Antiretroviral Therapy in Portugal, a Multicentric Study. Healthcare (Basel). 2021;9(7). Epub 2021/07/03. doi: 10.3390/healthcare9070797. PubMed PMID: 34202051; PubMed Central PMCID: PMCPMC8306717.
7. Deeks SG. HIV infection, inflammation, immunosenescence, and aging. Annu Rev Med. 2011;62:141-55. Epub 2010/11/26. doi: 10.1146/annurev-med-042909-093756. PubMed PMID: 21090961; PubMed Central PMCID: PMCPMC3759035.
8. Deeks SG, Lewin SR, Havlir DV. The end of AIDS: HIV infection as a chronic disease. Lancet. 2013;382(9903):1525-33. Epub 2013/10/25. doi: 10.1016/S0140-6736(13)61809-7. PubMed PMID: 24152939; PubMed Central PMCID: PMCPMC4058441.
9. Ellis RJ, Badiee J, Vaida F, Letendre S, Heaton RK, Clifford D, et al. CD4 nadir is a predictor of HIV neurocognitive impairment in the era of combination antiretroviral therapy. AIDS. 2011;25(14):1747-51. doi: 10.1097/QAD.0b013e32834a40cd. PubMed PMID: 21750419; PubMed Central PMCID: PMCPMC3867631.
10. Heaton RK, Clifford DB, Franklin DR, Jr., Woods SP, Ake C, Vaida F, et al. HIV-associated neurocognitive disorders persist in the era of potent antiretroviral therapy: CHARTER Study. Neurology. 2010;75(23):2087-96. doi: 10.1212/WNL.0b013e318200d727. PubMed PMID: 21135382; PubMed Central PMCID: PMCPMC2995535.
11. Peluso MJ, Meyerhoff DJ, Price RW, Peterson J, Lee E, Young AC, et al. Cerebrospinal fluid and neuroimaging biomarker abnormalities suggest early neurological injury in a subset of individuals during primary HIV infection. J Infect Dis. 2013;207(11):1703-12. doi: 10.1093/infdis/jit088. PubMed PMID: 23460748; PubMed Central PMCID: PMCPMC3636785.
12. Wright EJ, Grund B, Cysique LA, Robertson KR, Brew BJ, Collins G, et al. Factors associated with neurocognitive test performance at baseline: a substudy of the INSIGHT Strategic Timing of AntiRetroviral Treatment (START) trial. HIV Med. 2015;16 Suppl 1:97-108. doi: 10.1111/hiv.12238. PubMed PMID: 25711328.
13. Antinori A, Arendt G, Becker JT, Brew BJ, Byrd DA, Cherner M, et al. Updated research nosology for HIV-associated neurocognitive disorders. Neurology. 2007;69(18):1789-99. Epub

2007/10/05. doi: 10.1212/01.WNL.0000287431.88658.8b. PubMed PMID: 17914061; PubMed Central PMCID: PMCPMC4472366.
14. Wang Y, Liu M, Lu Q, Farrell M, Lappin JM, Shi J, et al. Global prevalence and burden of HIV-associated neurocognitive disorder: A meta-analysis. Neurology. 2020;95(19):e2610-e21. Epub 2020/09/06. doi: 10.1212/WNL.0000000000010752. PubMed PMID: 32887786.
15. McArthur JC, Steiner J, Sacktor N, Nath A. Human immunodeficiency virus-associated neurocognitive disorders: Mind the gap. Ann Neurol. 2010;67(6):699-714. Epub 2010/06/03. doi: 10.1002/ana.22053. PubMed PMID: 20517932.
16. Nightingale S, Ances B, Cinque P, Dravid A, Dreyer AJ, Gisslen M, et al. Cognitive impairment in people living with HIV: consensus recommendations for a new approach. Nat Rev Neurol. 2023;19(7):424-33. Epub 2023/06/14. doi: 10.1038/s41582-023-00813-2. PubMed PMID: 37311873.
17. Wiley CA, Schrier RD, Nelson JA, Lampert PW, Oldstone MB. Cellular localization of human immunodeficiency virus infection within the brains of acquired immune deficiency syndrome patients. Proc Natl Acad Sci U S A. 1986;83(18):7089-93. Epub 1986/09/01. doi: 10.1073/pnas.83.18.7089. PubMed PMID: 3018755; PubMed Central PMCID: PMCPMC386658.
18. Wiley CA, Nelson JA. Role of human immunodeficiency virus and cytomegalovirus in AIDS encephalitis. Am J Pathol. 1988;133(1):73-81. Epub 1988/10/01. PubMed PMID: 2845792; PubMed Central PMCID: PMCPMC1880646.
19. Staprans S, Marlowe N, Glidden D, Novakovic-Agopian T, Grant RM, Heyes M, et al. Time course of cerebrospinal fluid responses to antiretroviral therapy: evidence for variable compartmentalization of infection. AIDS. 1999;13(9):1051-61. Epub 1999/07/09. doi: 10.1097/00002030-199906180-00008. PubMed PMID: 10397535.
20. Schnell G, Spudich S, Harrington P, Price RW, Swanstrom R. Compartmentalized human immunodeficiency virus type 1 originates from long-lived cells in some subjects with HIV-1-associated dementia. PLoS Pathog. 2009;5(4):e1000395. Epub 2009/04/25. doi: 10.1371/journal.ppat.1000395. PubMed PMID: 19390619; PubMed Central PMCID: PMCPMC2668697.
21. Sharer LR, Baskin GB, Cho ES, Murphey-Corb M, Blumberg BM, Epstein LG. Comparison of simian immunodeficiency virus and human immunodeficiency virus encephalitides in the immature host. Ann Neurol. 1988;23 Suppl:S108-12. Epub 1988/01/01. doi: 10.1002/ana.410230727. PubMed PMID: 2831797.
22. Clements JE, Mankowski JL, Gama L, Zink MC. The accelerated simian immunodeficiency virus macaque model of human immunodeficiency virus-associated neurological disease: from mechanism to treatment. J Neurovirol. 2008;14(4):309-17. Epub 2008/09/10. doi: 10.1080/13550280802132832. PubMed PMID: 18780232; PubMed Central PMCID: PMCPMC8797541.
23. Byrnes SJ, Angelovich TA, Busman-Sahay K, Cochrane CR, Roche M, Estes JD, et al. Non-Human Primate Models of HIV Brain Infection and Cognitive Disorders. Viruses. 2022;14(9). Epub 2022/09/24. doi: 10.3390/v14091997. PubMed PMID: 36146803; PubMed Central PMCID: PMCPMC9500831.
24. Williams K, Westmoreland S, Greco J, Ratai E, Lentz M, Kim WK, et al. Magnetic resonance spectroscopy reveals that activated monocytes contribute to neuronal injury in SIV neuroAIDS. J Clin Invest. 2005;115(9):2534-45. Epub 2005/08/20. doi: 10.1172/jci22953. PubMed PMID: 16110325; PubMed Central PMCID: PMCPMC1187930.
25. Matsuda K, Riddick NE, Lee CA, Puryear SB, Wu F, Lafont BAP, et al. A SIV molecular clone that targets the CNS and induces neuroAIDS in rhesus macaques. PLoS Pathog. 2017;13(8):e1006538. Epub 2017/08/09. doi: 10.1371/journal.ppat.1006538. PubMed PMID: 28787449; PubMed Central PMCID: PMCPMC5560746.
26. Letendre SL, Mills AM, Tashima KT, Thomas DA, Min SS, Chen S, et al. ING116070: a study of the pharmacokinetics and antiviral activity of dolutegravir in cerebrospinal fluid in HIV-1-

1168 infected, antiretroviral therapy-naive subjects. Clin Infect Dis. 2014;59(7):1032-7. Epub
1169 2014/06/20. doi: 10.1093/cid/ciu477. PubMed PMID: 24944232; PubMed Central PMCID:
1170 PMCPMC4166983.
1171 27. Calcagno A, Bonora S, Simiele M, Rostagno R, Tettoni MC, Bonasso M, et al. Tenofovir
1172 and emtricitabine cerebrospinal fluid-to-plasma ratios correlate to the extent of blood-brainbarrier
1173 damage. AIDS. 2011;25(11):1437-9. Epub 2011/06/30. doi: 10.1097/QAD.0b013e3283489cb1.
1174 PubMed PMID: 21712657.
1175 28. Decloedt EH, Rosenkranz B, Maartens G, Joska J. Central nervous system penetration of
1176 antiretroviral drugs: pharmacokinetic, pharmacodynamic and pharmacogenomic considerations.
1177 Clin Pharmacokinet. 2015;54(6):581-98. Epub 2015/03/18. doi: 10.1007/s40262-015-0257-3.
1178 PubMed PMID: 25777740.
1179 29. Letendre S, Marquie-Beck J, Capparelli E, Best B, Clifford D, Collier AC, et al. Validation
1180 of the CNS Penetration-Effectiveness rank for quantifying antiretroviral penetration into the central
1181 nervous system. Arch Neurol. 2008;65(1):65-70. Epub 2008/01/16. doi:
1182 10.1001/archneurol.2007.31. PubMed PMID: 18195140; PubMed Central PMCID:
1183 PMCPMC2763187.
1184 30. Hedlund G, Sandberg-Wollheim M, Sjogren HO. Increased proportion of
1185 CD4+CDw29+CD45R-UCHL-1+ lymphocytes in the cerebrospinal fluid of both multiple sclerosis
1186 patients and healthy individuals. Cell Immunol. 1989;118(2):406-12. Epub 1989/02/01. doi:
1187 10.1016/0008-8749(89)90388-2. PubMed PMID: 2562931.
1188 31. Margolick JB, McArthur JC, Scott ER, McArthur JH, Cohn S, Farzadegan H, et al. Flow
1189 cytometric quantitation of T cell phenotypes in cerebrospinal fluid and peripheral blood of
1190 homosexual men with and without antibodies to human immunodeficiency virus, type I. J
1191 Neuroimmunol. 1988;20(1):73-81. Epub 1988/11/01. doi: 10.1016/0165-5728(88)90116-6.
1192 PubMed PMID: 3263391.
1193 32. Sharma V, Creegan M, Tokarev A, Hsu D, Slike BM, Sacdalan C, et al. Cerebrospinal fluid
1194 CD4+ T cell infection in humans and macaques during acute HIV-1 and SHIV infection. PLoS
1195 Pathog. 2021;17(12):e1010105. Epub 2021/12/08. doi: 10.1371/journal.ppat.1010105. PubMed
1196 PMID: 34874976; PubMed Central PMCID: PMCPMC8683024.
1197 33. Goertz JE, Garcia-Bonilla L, Iadecola C, Anrather J. Immune compartments at the brain's
1198 borders in health and neurovascular diseases. Semin Immunopathol. 2023;45(3):437-49. Epub
1199 2023/05/04. doi: 10.1007/s00281-023-00992-6. PubMed PMID: 37138042; PubMed Central
1200 PMCID: PMCPMC10279585.
1201 34. Louveau A, Plog BA, Antila S, Alitalo K, Nedergaard M, Kipnis J. Understanding the
1202 functions and relationships of the glymphatic system and meningeal lymphatics. J Clin Invest.
1203 2017;127(9):3210-9. Epub 2017/09/02. doi: 10.1172/jci90603. PubMed PMID: 28862640;
1204 PubMed Central PMCID: PMCPMC5669566 exists.
1205 35. Lun MP, Monuki ES, Lehtinen MK. Development and functions of the choroid plexus–
1206 cerebrospinal fluid system. Nature Reviews Neuroscience. 2015;16(8):445-57. doi:
1207 10.1038/nrn3921.
1208 36. Zhou X, Yu S, Zhao DM, Harty JT, Badovinac VP, Xue HH. Differentiation and persistence
1209 of memory CD8(+) T cells depend on T cell factor 1. Immunity. 2010;33(2):229-40. Epub
1210 2010/08/24. doi: 10.1016/j.immuni.2010.08.002. PubMed PMID: 20727791; PubMed Central
1211 PMCID: PMCPMC2928475.
1212 37. Ram DR, Manickam C, Hueber B, Itell HL, Permar SR, Varner V, et al. Tracking KLRC2
1213 (NKG2C)+ memory-like NK cells in SIV+ and rhCMV+ rhesus macaques. PLoS Pathog.
1214 2018;14(5):e1007104. Epub 2018/06/01. doi: 10.1371/journal.ppat.1007104. PubMed PMID:
1215 29851983; PubMed Central PMCID: PMCPMC5997355.
1216 38. Sichien D, Scott CL, Martens L, Vanderkerken M, Van Gassen S, Plantinga M, et al. IRF8
1217 Transcription Factor Controls Survival and Function of Terminally Differentiated Conventional and

1218 Plasmacytoid Dendritic Cells, Respectively. Immunity. 2016;45(3):626-40. Epub 2016/09/18. doi:
1219 10.1016/j.immuni.2016.08.013. PubMed PMID: 27637148.
1220 39. Jurczyszak D, Manganaro L, Buta S, Gruber C, Martin-Fernandez M, Taft J, et al. ISG15
1221 deficiency restricts HIV-1 infection. PLoS Pathog. 2022;18(3):e1010405. Epub 2022/03/26. doi:
1222 10.1371/journal.ppat.1010405. PubMed PMID: 35333911; PubMed Central PMCID:
1223 PMCPMC8986114 following competing interests: DB is founder and part owner of Lab11
1224 Therapeutics Inc.
1225 40. Hsu YL, Shi SF, Wu WL, Ho LJ, Lai JH. Protective roles of interferon-induced protein with
1226 tetratricopeptide repeats 3 (IFIT3) in dengue virus infection of human lung epithelial cells. PLoS
1227 One. 2013;8(11):e79518. Epub 2013/11/14. doi: 10.1371/journal.pone.0079518. PubMed PMID:
1228 24223959; PubMed Central PMCID: PMCPMC3817122.
1229 41. Berger G, Durand S, Fargier G, Nguyen XN, Cordeil S, Bouaziz S, et al. APOBEC3A is a
1230 specific inhibitor of the early phases of HIV-1 infection in myeloid cells. PLoS Pathog.
1231 2011;7(9):e1002221. Epub 2011/10/04. doi: 10.1371/journal.ppat.1002221. PubMed PMID:
1232 21966267; PubMed Central PMCID: PMCPMC3178557.
1233 42. Dominguez CX, Amezquita RA, Guan T, Marshall HD, Joshi NS, Kleinstein SH, et al. The
1234 transcription factors ZEB2 and T-bet cooperate to program cytotoxic T cell terminal differentiation
1235 in response to LCMV viral infection. J Exp Med. 2015;212(12):2041-56. Epub 2015/10/28. doi:
1236 10.1084/jem.20150186. PubMed PMID: 26503446; PubMed Central PMCID: PMCPMC4647261.
1237 43. van der Leun AM, Thommen DS, Schumacher TN. CD8(+) T cell states in human cancer:
1238 insights from single-cell analysis. Nat Rev Cancer. 2020;20(4):218-32. Epub 2020/02/07. doi:
1239 10.1038/s41568-019-0235-4. PubMed PMID: 32024970; PubMed Central PMCID:
1240 PMCPMC7115982.
1241 44. Batterman KV, Cabrera PE, Moore TL, Rosene DL. T Cells Actively Infiltrate the White
1242 Matter of the Aging Monkey Brain in Relation to Increased Microglial Reactivity and Cognitive
1243 Decline. Front Immunol. 2021;12:607691. Epub 2021/03/06. doi: 10.3389/fimmu.2021.607691.
1244 PubMed PMID: 33664743; PubMed Central PMCID: PMCPMC7920950.
1245 45. Stout JC, Ellis RJ, Jernigan TL, Archibald SL, Abramson I, Wolfson T, et al. Progressive
1246 Cerebral Volume Loss in Human Immunodeficiency Virus Infection: A Longitudinal Volumetric
1247 Magnetic Resonance Imaging Study. Archives of Neurology. 1998;55(2):161-8. doi:
1248 10.1001/archneur.55.2.161.
1249 46. Underwood J, Cole JH, Caan M, De Francesco D, Leech R, van Zoest RA, et al. Gray and
1250 White Matter Abnormalities in Treated Human Immunodeficiency Virus Disease and Their
1251 Relationship to Cognitive Function. Clin Infect Dis. 2017;65(3):422-32. Epub 2017/04/08. doi:
1252 10.1093/cid/cix301. PubMed PMID: 28387814; PubMed Central PMCID: PMCPMC5850629.
1253 47. Schnell G, Joseph S, Spudich S, Price RW, Swanstrom R. HIV-1 replication in the central
1254 nervous system occurs in two distinct cell types. PLoS Pathog. 2011;7(10):e1002286. Epub
1255 2011/10/19. doi: 10.1371/journal.ppat.1002286. PubMed PMID: 22007152; PubMed Central
1256 PMCID: PMCPMC3188520.
1257 48. Carvalhal A, Gill MJ, Letendre SL, Rachlis A, Bekele T, Raboud J, et al. Central nervous
1258 system penetration effectiveness of antiretroviral drugs and neuropsychological impairment in the
1259 Ontario HIV Treatment Network Cohort Study. J Neurovirol. 2016;22(3):349-57. Epub 2015/11/18.
1260 doi: 10.1007/s13365-015-0404-5. PubMed PMID: 26572786.
1261 49. Hsiao F, Frouard J, Gramatica A, Xie G, Telwatte S, Lee GQ, et al. Tissue memory CD4+
1262 T cells expressing IL-7 receptor-alpha (CD127) preferentially support latent HIV-1 infection. PLoS
1263 Pathog. 2020;16(4):e1008450. Epub 2020/05/01. doi: 10.1371/journal.ppat.1008450. PubMed
1264 PMID: 32353080; PubMed Central PMCID: PMCPMC7192375.
1265 50. Parrish NF, Wilen CB, Banks LB, Iyer SS, Pfaff JM, Salazar-Gonzalez JF, et al.
1266 Transmitted/founder and chronic subtype C HIV-1 use CD4 and CCR5 receptors with equal
1267 efficiency and are not inhibited by blocking the integrin alpha4beta7. PLoS Pathog.

2012;8(5):e1002686. Epub 2012/06/14. doi: 10.1371/journal.ppat.1002686. PubMed PMID: 22693444; PubMed Central PMCID: PMCPMC3364951.
51. Gray JI, Farber DL. Tissue-Resident Immune Cells in Humans. Annu Rev Immunol. 2022;40:195-220. Epub 2022/01/20. doi: 10.1146/annurev-immunol-093019-112809. PubMed PMID: 35044795.
52. Sallusto F, Lenig D, Forster R, Lipp M, Lanzavecchia A. Two subsets of memory T lymphocytes with distinct homing potentials and effector functions. Nature. 1999;401(6754):708-12. Epub 1999/10/28. doi: 10.1038/44385. PubMed PMID: 10537110.
53. Smolders J, Heutinck KM, Fransen NL, Remmerswaal EBM, Hombrink P, ten Berge IJM, et al. Tissue-resident memory T cells populate the human brain. Nature Communications. 2018;9(1):4593. doi: 10.1038/s41467-018-07053-9.
54. Kumar BV, Ma W, Miron M, Granot T, Guyer RS, Carpenter DJ, et al. Human Tissue-Resident Memory T Cells Are Defined by Core Transcriptional and Functional Signatures in Lymphoid and Mucosal Sites. Cell Rep. 2017;20(12):2921-34. Epub 2017/09/21. doi: 10.1016/j.celrep.2017.08.078. PubMed PMID: 28930685; PubMed Central PMCID: PMCPMC5646692.
55. Eberlein J, Davenport B, Nguyen TT, Victorino F, Jhun K, van der Heide V, et al. Chemokine Signatures of Pathogen-Specific T Cells I: Effector T Cells. J Immunol. 2020;205(8):2169-87. Epub 2020/09/20. doi: 10.4049/jimmunol.2000253. PubMed PMID: 32948687; PubMed Central PMCID: PMCPMC7541659.
56. Zanoni M, Palesch D, Pinacchio C, Statzu M, Tharp GK, Paiardini M, et al. Innate, non-cytolytic CD8+ T cell-mediated suppression of HIV replication by MHC-independent inhibition of virus transcription. PLoS Pathog. 2020;16(9):e1008821. Epub 2020/09/18. doi: 10.1371/journal.ppat.1008821. PubMed PMID: 32941545; PubMed Central PMCID: PMCPMC7523993.
57. Sturdevant CB, Joseph SB, Schnell G, Price RW, Swanstrom R, Spudich S. Compartmentalized replication of R5 T cell-tropic HIV-1 in the central nervous system early in the course of infection. PLoS Pathog. 2015;11(3):e1004720. Epub 2015/03/27. doi: 10.1371/journal.ppat.1004720. PubMed PMID: 25811757; PubMed Central PMCID: PMCPMC4374811.
58. Lustig G, Cele S, Karim F, Derache A, Ngoepe A, Khan K, et al. T cell derived HIV-1 is present in the CSF in the face of suppressive antiretroviral therapy. PLoS Pathog. 2021;17(9):e1009871. Epub 2021/09/24. doi: 10.1371/journal.ppat.1009871. PubMed PMID: 34555123; PubMed Central PMCID: PMCPMC8509856 Ntshuba was unable to confirm their authorship contributions. On their behalf, the corresponding author has reported their contributions to the best of their knowledge.
59. Rustenhoven J, Drieu A, Mamuladze T, de Lima KA, Dykstra T, Wall M, et al. Functional characterization of the dural sinuses as a neuroimmune interface. Cell. 2021;184(4):1000-16.e27. Epub 2021/01/29. doi: 10.1016/j.cell.2020.12.040. PubMed PMID: 33508229; PubMed Central PMCID: PMCPMC8487654.
60. Cugurra A, Mamuladze T, Rustenhoven J, Dykstra T, Beroshvili G, Greenberg ZJ, et al. Skull and vertebral bone marrow are myeloid cell reservoirs for the meninges and CNS parenchyma. Science. 2021;373(6553). Epub 2021/06/05. doi: 10.1126/science.abf7844. PubMed PMID: 34083447; PubMed Central PMCID: PMCPMC8863069.
61. Herisson F, Frodermann V, Courties G, Rohde D, Sun Y, Vandoorne K, et al. Direct vascular channels connect skull bone marrow and the brain surface enabling myeloid cell migration. Nat Neurosci. 2018;21(9):1209-17. Epub 2018/08/29. doi: 10.1038/s41593-018-0213-2. PubMed PMID: 30150661; PubMed Central PMCID: PMCPMC6148759.
62. Tang Y, Chaillon A, Gianella S, Wong LM, Li D, Simermeyer TL, et al. Brain microglia serve as a persistent HIV reservoir despite durable antiretroviral therapy. J Clin Invest.

2023;133(12). Epub 2023/06/15. doi: 10.1172/jci167417. PubMed PMID: 37317962; PubMed Central PMCID: PMCPMC10266791.

63. Colton CA. Heterogeneity of microglial activation in the innate immune response in the brain. J Neuroimmune Pharmacol. 2009;4(4):399-418. Epub 2009/08/06. doi: 10.1007/s11481-009-9164-4. PubMed PMID: 19655259; PubMed Central PMCID: PMCPMC2773116.

64. Ta TT, Dikmen HO, Schilling S, Chausse B, Lewen A, Hollnagel JO, et al. Priming of microglia with IFN-gamma slows neuronal gamma oscillations in situ. Proc Natl Acad Sci U S A. 2019;116(10):4637-42. Epub 2019/02/21. doi: 10.1073/pnas.1813562116. PubMed PMID: 30782788; PubMed Central PMCID: PMCPMC6410786.

65. Colonna M, Butovsky O. Microglia Function in the Central Nervous System During Health and Neurodegeneration. Annu Rev Immunol. 2017;35:441-68. Epub 2017/02/23. doi: 10.1146/annurev-immunol-051116-052358. PubMed PMID: 28226226; PubMed Central PMCID: PMCPMC8167938.

66. Del Prete GQ, Smedley J, Macallister R, Jones GS, Li B, Hattersley J, et al. Short Communication: Comparative Evaluation of Coformulated Injectable Combination Antiretroviral Therapy Regimens in Simian Immunodeficiency Virus-Infected Rhesus Macaques. AIDS Res Hum Retroviruses. 2016;32(2):163-8. Epub 2015/07/08. doi: 10.1089/aid.2015.0130. PubMed PMID: 26150024; PubMed Central PMCID: PMCPMC4761795.

67. Hansen SG, Piatak M, Jr., Ventura AB, Hughes CM, Gilbride RM, Ford JC, et al. Immune clearance of highly pathogenic SIV infection. Nature. 2013;502(7469):100-4. Epub 2013/09/13. doi: 10.1038/nature12519. PubMed PMID: 24025770; PubMed Central PMCID: PMCPMC3849456.

68. Devanathan AS, Fallon JK, White NR, Schauer AP, Van Horne B, Blake K, et al. Antiretroviral Penetration and Drug Transporter Concentrations in the Spleens of Three Preclinical Animal Models and Humans. Antimicrob Agents Chemother. 2020;64(10). Epub 2020/07/15. doi: 10.1128/AAC.01384-20. PubMed PMID: 32661005; PubMed Central PMCID: PMCPMC7508597.

69. Hawes CE, Elizaldi SR, Beckman D, Diniz GB, Shaan Lakshmanappa Y, Ott S, et al. Neuroinflammatory transcriptional programs induced in rhesus pre-frontal cortex white matter during acute SHIV infection. J Neuroinflammation. 2022;19(1):250. Epub 2022/10/07. doi: 10.1186/s12974-022-02610-y. PubMed PMID: 36203187; PubMed Central PMCID: PMCPMC9535930.

70. Verma A, Schmidt BA, Elizaldi SR, Nguyen NK, Walter KA, Beck Z, et al. Impact of T(h)1 CD4 Follicular Helper T Cell Skewing on Antibody Responses to an HIV-1 Vaccine in Rhesus Macaques. J Virol. 2020;94(6). Epub 2019/12/13. doi: 10.1128/JVI.01737-19. PubMed PMID: 31827000; PubMed Central PMCID: PMCPMC7158739.

71. Ma ZM, Miller CJ. Immunophenotype of simian immunodeficiency virus-infected cells in the spleen of a rhesus monkey. AIDS Res Hum Retroviruses. 2015;31(4):359-60. Epub 2015/03/12. doi: 10.1089/aid.2014.0343. PubMed PMID: 25760311; PubMed Central PMCID: PMCPMC4378854.

**Figures.**

**Figure. 1**

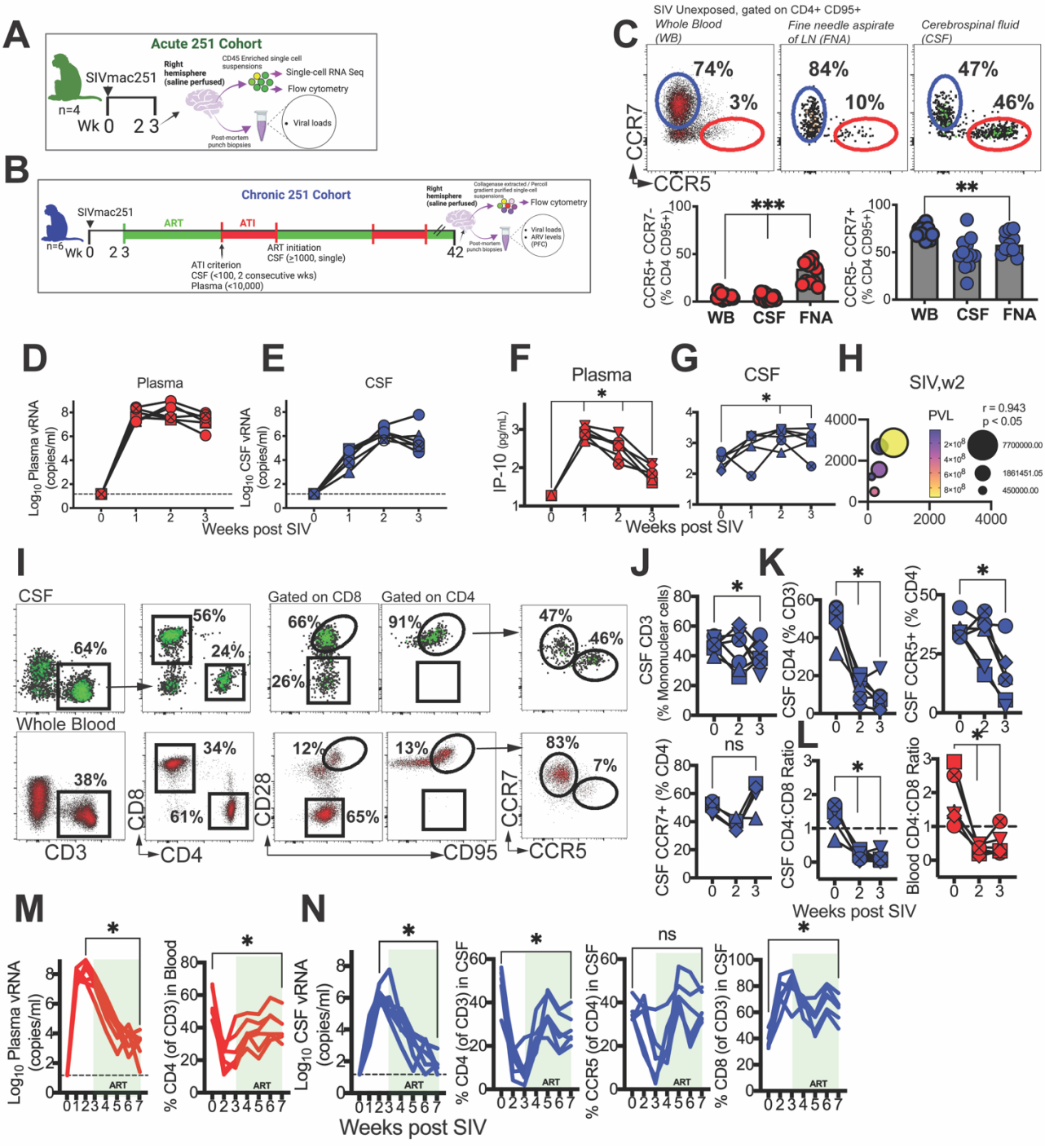

**Figure. 2**

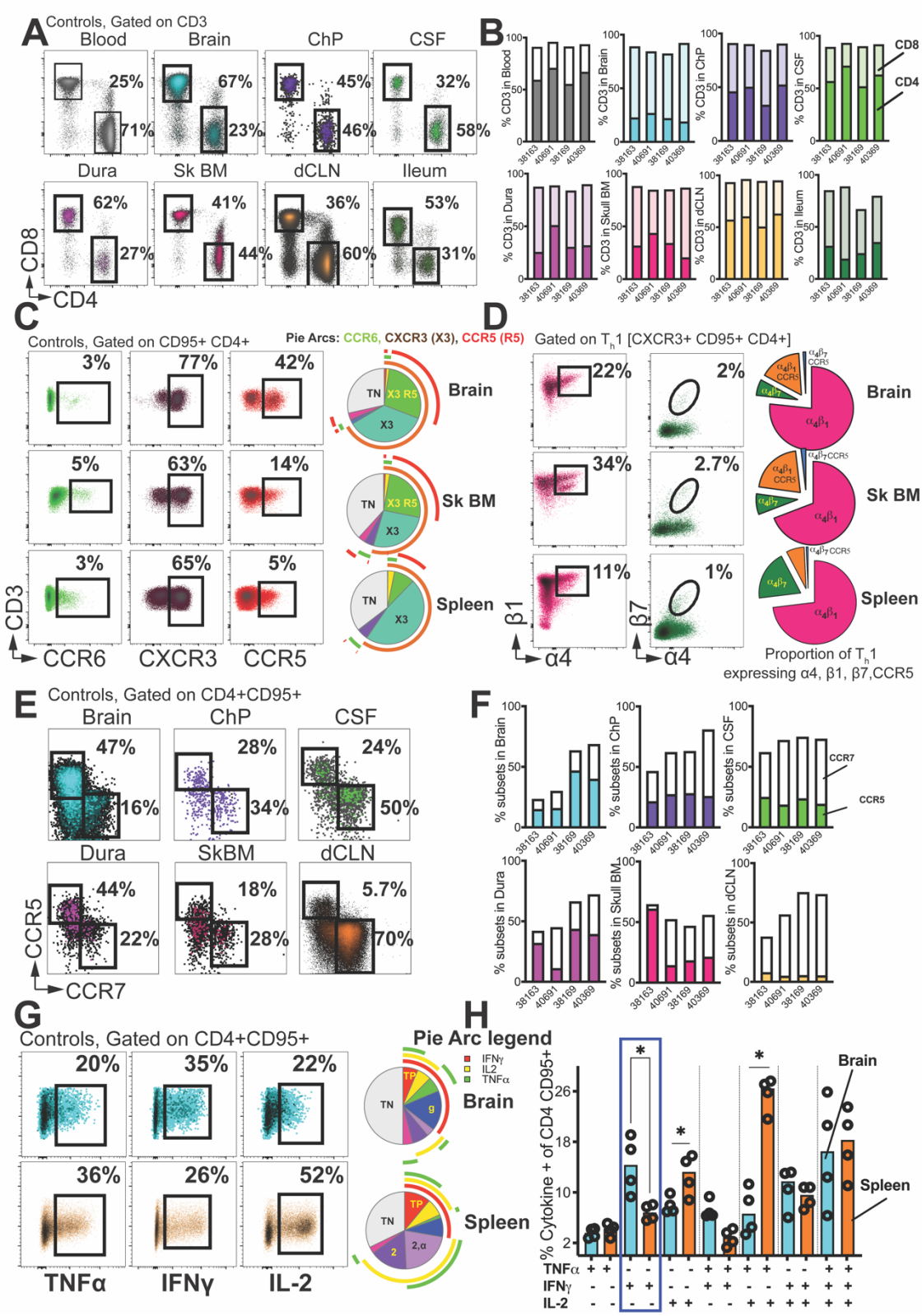

**Figure. 3**

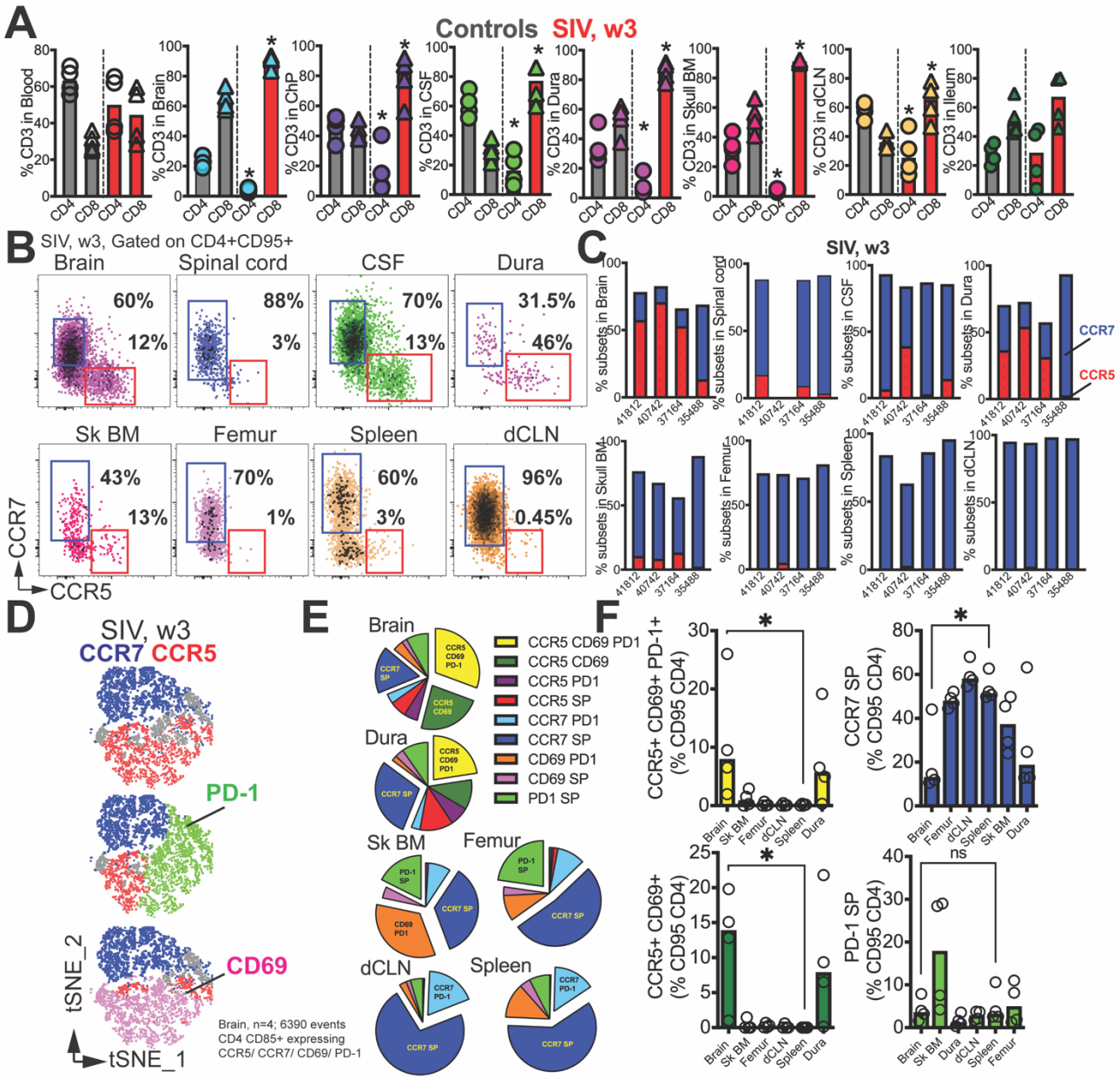

**Figure. 4**

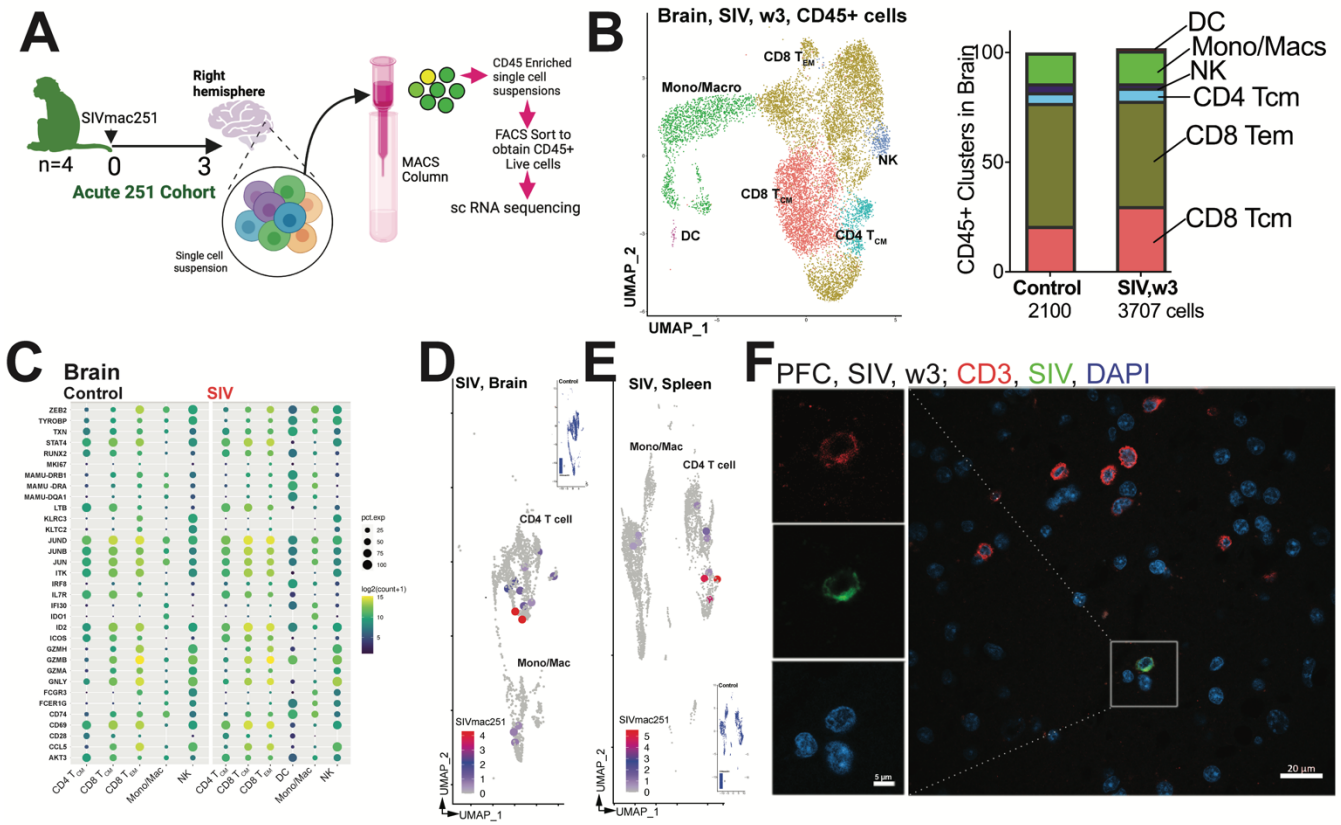

**Figure. 5**

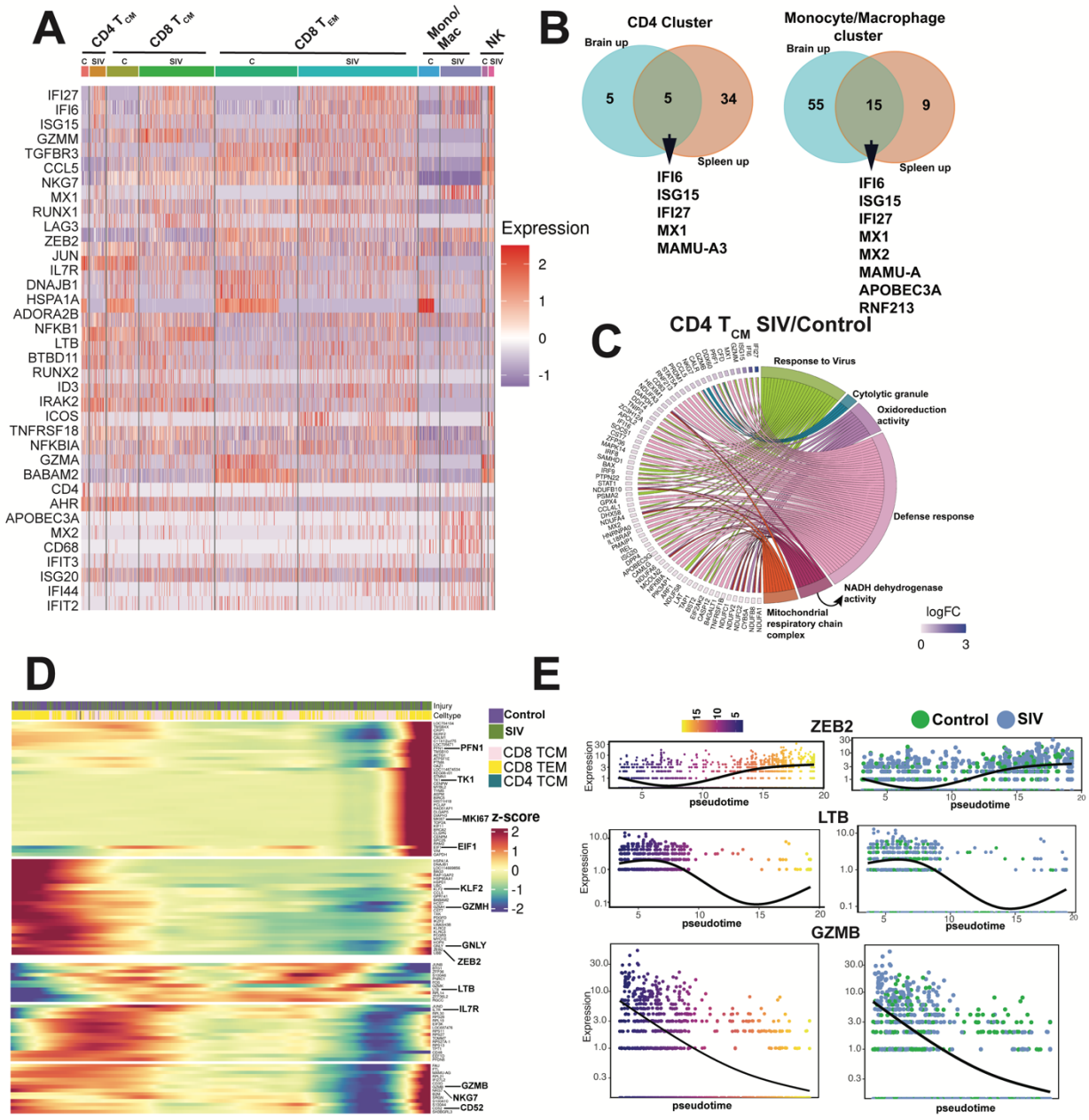

**Figure. 6**

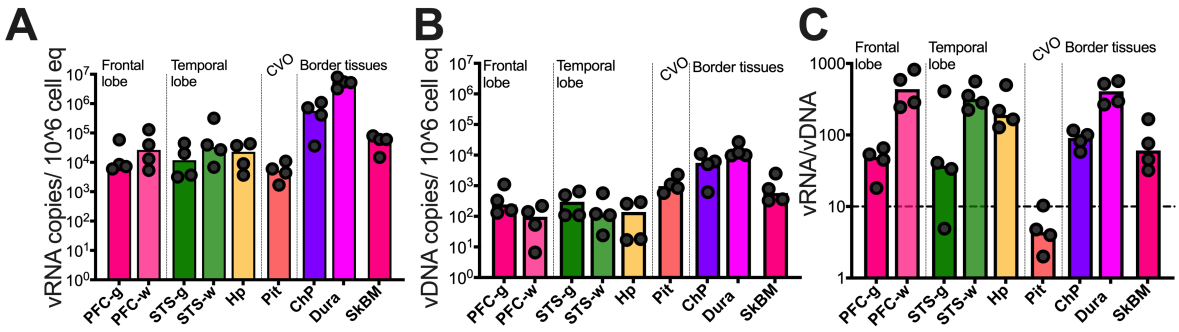


**Figure. 7**

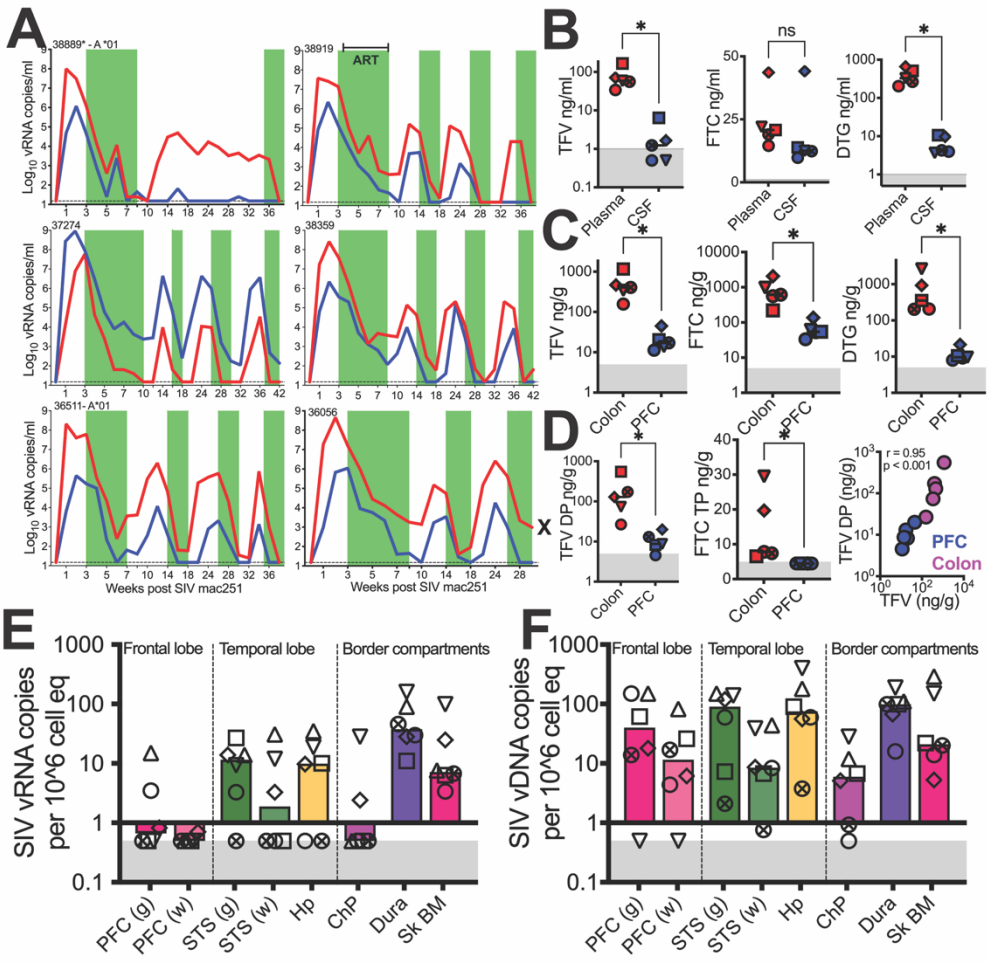

**Figure. 8**